

The 2018 phreatic eruption at Mt. Motoshirane of Kusatsu–Shirane volcano, Japan: Eruption and intrusion of hydrothermal fluid observed by a borehole tiltmeter network

Akihiko Terada (✉ terada@ksvo.titech.ac.jp)

Volcanic Fluid Research Center, School of Science, Tokyo Institute of Technology

<https://orcid.org/0000-0001-5746-4912>

Wataru Kanda

Volcanic Fluid Research Center, School of Science, Tokyo Institute of Technology

Yasuo Ogawa

Volcanic Fluid Research Center, School of Science, Tokyo Institute of Technology

Taishi Yamada

Sakurajima Volcano Research Center, Disaster Prevention Research Center, Kyoto University

Mare Yamamoto

Graduate School of Science, Tohoku University

Takahiro Ohkura

Aso Volcanological Laboratory, Kyoto University

Hiroshi Aoyama

Institute of Seismology and volcanology, Faculty of Science, Hokkaido University

Tsutsui Tomoki

Sakurajima Volcano Research Center, Disaster Prevention Research Institute, Kyoto University

Shin'ya Onizawa

Volcanology Research Department, Meteorological Research Institute, Japan Meteorological Agency

Research Article

Keywords: Phreatic eruption, tiltmeter, Kusatsu-Shirane volcano, hydrothermal system, tensile crack, brittle-ductile transition zone

Posted Date: June 2nd, 2021

DOI: <https://doi.org/10.21203/rs.3.rs-285566/v1>

License:  This work is licensed under a Creative Commons Attribution 4.0 International License.

[Read Full License](#)

Version of Record: A version of this preprint was published at Earth, Planets and Space on July 30th, 2021. See the published version at <https://doi.org/10.1186/s40623-021-01475-4>.

1 **Title: The 2018 phreatic eruption at Mt. Motoshirane of Kusatsu–Shirane volcano,**
2 **Japan: Eruption and intrusion of hydrothermal fluid observed by a borehole**
3 **tiltmeter network**

4
5 Author #1: Akihiko Terada, Volcanic Fluid Research Center, School of Science, Tokyo
6 Institute of Technology, 2-12-1 Ookayama, Meguro, Tokyo 152-8551,
7 Japan, terada@ksvo.titech.ac.jp

8 Author #2: Wataru Kanda, Volcanic Fluid Research Center, School of Science, Tokyo
9 Institute of Technology, 2-12-1 Ookayama, Meguro, Tokyo 152-8551,
10 Japan, kanda@ksvo.titech.ac.jp

11 Author #3: Yasuo Ogawa, Volcanic Fluid Research Center, School of Science, Tokyo
12 Institute of Technology, 2-12-1 Ookayama, Meguro, Tokyo 152-8551,
13 Japan, oga@ksvo.titech.ac.jp

14 Author #4: Taishi Yamada, Sakurajima Volcano Research Center, Disaster Prevention
15 Research Institute, Kyoto University, 1722-19 Sakurajima-Yokoyama,
16 Kagoshima 891-1419, Japan, yamada.taishi.8m@kyoto-u.ac.jp

17 Author #5: Mare Yamamoto, Graduate School of Science, Tohoku University, 6-6,
18 Aramaki-aza-Aoba, Aoba-ku, Sendai 980-8578, Japan, mare@tohoku.ac.jp

19 Author #6: Takahiro Ohkura, Aso Volcanological Laboratory, Kyoto University, 5280
20 Kawayo, Minami-Aso, Kumamoto 869-1404, Japan,
21 bonkura@aso.vgs.kyoto-u.ac.jp

22 Author #7: Hiroshi Aoyama, Institute of Seismology and Volcanology, Faculty of
23 Science, Hokkaido University, N10W8, Kita-ku, Sapporo, Hokkaido
24 060-0810, Japan, aoyama@sci.hokudai.ac.jp

25 Author #8: Tomoki Tsutsui, Sakurajima Volcano Research Center, Disaster Prevention
26 Research Institute, Kyoto University, 1722-19 Sakurajima-Yokoyama,
27 Kagoshima 891-1419, Japan, tsutsui.tomoki.8x@kyoto-u.ac.jp

28 Author #9: Shin'ya Onizawa, Volcanology Research Department, Meteorological
29 Research Institute, Japan Meteorological Agency, 1-1 Nagamine, Tsukuba,
30 Ibaraki 305-0052, Japan, sonizawa@mri-jma.go.jp

31

32 **Indicate the corresponding author**

33 Akihiko Terada, Volcanic Fluid Research Center, School of Science, Tokyo Institute of

34 Technology Tokyo, JAPAN, terada@ksvo.titech.ac.jp

35

36

37 **Abstract**

38 We estimate the mass and energy budgets for the 2018 phreatic eruption of Mt.
39 Motoshirane on Kusatsu–Shirane volcano, Japan, based on data obtained from a network
40 of eight tiltmeters and weather radar echoes. The tilt records can be explained by a
41 subvertical crack model. Small craters that were formed by previous eruptions are aligned
42 WNW–ESE, which is consistent with the crack azimuth modeled in this study. The
43 direction of maximum compressive stress in this region is horizontal and oriented WNW–
44 ESE, allowing fluid to intrude from depth through a crack with this orientation. Based on
45 the crack model, hypocenter distribution, and MT resistivity structure, we infer that fluid
46 from a hydrothermal reservoir at a depth of 2 km below Kusatsu–Shirane volcano has
47 repeatedly ascended through a pre-existing subvertical crack. The inflation and deflation
48 volumes during the 2018 eruption are estimated to have been 5.1×10^5 and 3.6×10^5
49 m^3 , respectively, meaning that $1.5 \times 10^5 \text{ m}^3$ of expanded volume formed underground.
50 The total heat associated with the expanded volume is estimated to have been $\geq 10^{14}$ J,
51 similar to or exceeding the annual heat released from Yugama Crater Lake of Mt. Shirane
52 and that from the largest eruption during the past 130 yr. Although the ejecta mass of the

53 2018 phreatic eruption was small, the 2018 MPCG eruption was not negligible in terms
54 of the energy budget of Kusatsu–Shirane volcano. A water mass of $0.1\text{--}2.0 \times 10^7$ kg
55 was discharged as a volcanic cloud, based on weather radar echoes, which is smaller than
56 the mass associated with the deflation. We suggest that underground water acted as a
57 buffer against the sudden intrusion of hydrothermal fluids, absorbing some of the fluid
58 that ascended through the crack.

59

60 **Keywords**

61 Phreatic eruption, tiltmeter, Kusatsu-Shirane volcano, hydrothermal system, tensile

62 crack, brittle-ductile transition zone

63

64

65 **1. Introduction**

66 In 2018, a phreatic eruption occurred on the Kagamiike-kita and Kagamiike
67 pyroclastic cone (PC) of the Mt. Motoshirane Pyroclastic Cones Group (MPCG) on the
68 southern part of Kusatsu–Shirane volcano, Japan (Ogawa et al. 2018; Yamada et al. 2021).
69 The total mass of the fall deposit is estimated to have been $\sim 3.0 \times 10^4$ tonne (Kametani
70 et al. submitted to this special issue). The eruption products were mainly clay minerals
71 derived from a high-temperature acid alteration zone beneath the volcano; no juvenile
72 material has been found (Yaguchi et al. 2019).

73 Until several minutes before the occurrence of the eruption, no significant
74 precursors (e.g., increased seismicity, seismic velocity change, unusual ground
75 deformation and unusual thermal activity) (Barberi et al. 1992) were detected around the
76 MPCG (Yamamoto et al. 2018). However, the Shirane Pyroclastic Cone Group (SPCG),
77 located 1.5 km north of the eruption site, exhibited an increase in seismicity, accompanied
78 by a shallow inflation of 1.2×10^5 m³ and changes in water chemistry of Yugama Crater
79 Lake (YCL) and nearby fumarolic gas from 2014 to 2016 (Ohba et al. 2019a). Moreover,
80 three months after the 2018 MPCG eruption, a shallow inflation and a marked increase

81 in seismicity occurred at the SPCG. Therefore, Kusatsu–Shirane volcano can be
82 categorized as a “persistently restless volcano” (Roman et al. 2019) or a “volcano with
83 slow unrest” (Stix 2018). Small craters formed by past phreatic eruptions occur
84 throughout the northern part of the MPCG, such as the Kagamiike-kita and Kagamiike
85 PC (Ishizaki et al. 2020). Thus, understanding the relationship between the hydrothermal
86 systems beneath the MPCG and SPCG can provide insights into the risk and processes
87 associated with a small phreatic eruption.

88 At the onset of the 2018 MPCG eruption, eight tiltmeters (including six
89 borehole-type; Fig. 1), including KSS located 1.2 km from the main crater (MC; Figs 1
90 and 2), were in operation at Kusatsu–Shirane volcano. Such a tiltmeter network with high
91 temporal resolution and dense spatial distribution provides details of progressive ground
92 deformation during an eruption (Ueda et al. 2013; Aloisi et al. 2019; Zobin et al. 2020).
93 Moreover, the volcanic ash cloud was monitored by weather radar (Meteorological
94 Research Institute 2018). The volcanic plume track allows the heat discharge rate of an
95 ash cloud to be estimated, which can then be converted to a mass flux of water (Briggs
96 1969; Kagiya 1981; Terada and Sudo 2012; Narita et al. 2019), although surveillance

97 cameras and photographs taken from the ground did not constrain the height of the ash
98 cloud at the climax of the eruption.

99 In this paper, we present a simple model of inflation–deflation during the 2018
100 MPCG eruption based on the tilt changes recorded at eight tiltmeter stations. In addition,
101 we estimate the mass of water discharged as an ash cloud. On the basis of these
102 estimations, we discuss the mass and energy budgets during the eruption. At Kusatsu–
103 Shirane volcano, the resistivity structure has been investigated by Magnetotelluric (MT)
104 sounding methods (Nurhasan et al. 2006; Matsunaga et al. 2020; Tseng et al. 2020). Such
105 a model of the underground structure provides a constraint of a fluid pathway beneath
106 Kusatsu-Shirane volcano. On the basis of the underground structure, the observations
107 during the eruption in 2018 at the MPCG and the progression of the unrest of the SPCG
108 since 2014, we propose a schematic model of the 2018 MPCG eruption.

109

110 **2. Kusatsu–Shirane volcano and the 2018 eruption**

111 Kusatsu–Shirane volcano consists of three pyroclastic cones (Figs 1 and 2a),
112 which are the SPCG, Ainomine Pyroclastic Cone (APC; undated but probably Holocene

113 in age), and MPCG that are aligned N–S over a distance of 4 km (Ishizaki et al. 2020).
114 Kusatsu–Shirane volcano exhibits a persistent heat release of 110 MW (Terada 2018),
115 which is transferred by a hyper-acidic, hot crater lake (locally referred to as YCL (Yugama
116 Crater Lake); Figs 1 and 2a; Ohba et al. 1994; Terada and Hashimoto 2017), nearby
117 fumaroles around the SPCG (Ohba et al. 2019a), and hot-spring water emissions on the
118 flank of the volcano. Phreatic eruptions have repeatedly occurred around the SPCG and,
119 as a result, the ground surface of the SPCG is covered with whitish tephra consisting of
120 clay and is unvegetated. The eruption series in 1937–1939 was the largest eruption in the
121 last 130 yr, and produced 5×10^9 kg of tephra (Minakami, 1939). The latest eruption of
122 the SPCG occurred at YCL in 1982–1983. Recently, microearthquake swarms
123 accompanied by ground deformation and changes in the chemistry of YCL and nearby
124 fumaroles were detected in 1991–1992 and 2014–2016 (Ohba et al. 2008, 2019b).

125 The MPCG was mostly covered by vegetation prior to the 2018 eruption (Figs.
126 1 and 2a). No eruption has been recorded in historic times, whereas continuous seismic
127 activity has been detected around the APC and MPCG (Mori et al. 2006). On 23 January
128 2018, a phreatic eruption occurred at Kagamike-kita PC (slightly younger than 1,500 cal.

129 yr BP) and Kagamiike PC (*ca.* 4,800 cal. yr BP), which are in the northern part of the
130 MPCG. The onset of eruption was preceded by ~2 min of volcanic tremor located 1 km
131 north of the MC (Fig. 2) at a depth of 0.5–1.0 km from the surface (Yamada et al. 2021).
132 The tremor was accompanied by rapid changes in tilt.

133 During the 2018 event, ballistic blocks fell up to 0.5 km from the MC and
134 resulted in one death. Volcanic ash released during the eruption was found up to 25 km
135 ENE of the volcano. The maximum height of the volcanic cloud was estimated to be
136 5,500 m asl by weather radar (Japan Meteorological Institute 2018), corresponding to
137 3,400 m in height relative to the altitude of the MC (Fig. 2). Eyewitness reports and
138 seismic records suggest that most of the ash emission had finished within ~10 min. A
139 photograph taken at around 10:20–10:30 (JST) from Kusatsu-town (Fig. 1) showed a
140 whitish plume and black tephra deposit around Kagamiike-kita PC, but no ash cloud (Fig.
141 2c). During the eruption, MC, west crater (WC), and other smaller craters were formed
142 on Kagamiike-kita PC (Fig. 2d), which are aligned on an azimuth of 112°. In addition,
143 south crater (SC) was formed on Kagamiike-kita PC (Fig. 2c) (Kametani et al. submitted
144 to this special issue).

145

146 **3. Tilt records during the 2018 eruption**

147 The Kusatsu–Shirane Volcano Observatory, Tokyo Institute of Technology
148 (KSVO) and the National Research Institute for Earth Science and Disaster Resilience
149 (NIED) operate force-balanced-type tiltmeters (Sato et al. 1980) at the present study site,
150 installed at the bottom of boreholes at depths of 50–200 m (Table 1). The output
151 sensitivity is 20 mV/ μ rad at KSE and KSW, and 5 mV/ μ rad at KSS, N.KSHV, N.KSYV,
152 and N.KSNV (Tanada et al. 2017), which produces a high tilt resolution of 10^{-8} – 10^{-9} μ rad.
153 Applied Geomechanics 701-2A dual-axis tiltmeters with an output sensitivity of 1
154 mV/ μ rad were deployed at depths of 2 and 1 m at JIE and YNW, respectively. The 701-
155 2A contains electrolytic level sensors that produce changes in resistance in response to a
156 rotation of the sensor. Tilt records are sampled at 20 Hz (NIED) or 200 Hz (KSVO). In
157 this study, acausal low-pass filters with cut-off frequencies of 0.034 Hz and 0.021 Hz
158 were applied to the tilt records of JTS-33 and 701-2A (Table 1), respectively. No data
159 were obtained for the N–S component at JIE owing to a mechanical problem. A tiltmeter
160 at V.KSAO, 1.6 km northeast of MC, operated by the Japan Meteorological Agency was

161 not operational when the 2018 eruption occurred but did record the 2011 event.

162

163 **3.1 Ground deformation detected by the tiltmeter network**

164 We detected a simple and significant variation in the tilt records from 10:00 (all
165 times are in Japan Standard Time) on 23 January 2018 (Fig. 3a). The largest change in
166 tilt of $16.3 \mu\text{rad}$ was observed at KSS located 1.2 km north of MC, followed by a change
167 at KSE of $12.7 \mu\text{rad}$. Tilt changes at the foot of the volcano (N.KSYV and N.KSNV) of
168 $0.1\text{--}0.9 \mu\text{rad}$ were somewhat complex, probably due to perturbation by long-period
169 events (Yamada et al. 2021). Vectors of tilt changes during the time period between 10:00
170 and 10:02 revealed a simple radial pattern from several hundred meters north of MC (Fig.
171 4a). After the onset of the eruption at 10:01:52 (Yamada et al. 2021), the vectors of the
172 tilt change reversed during the inflation period. The speed of the tilt changes gradually
173 decreased, and thus the timing of cessation of the tilt changes is uncertain. We assumed
174 that tilt changes after 10:20 were negligible. In this study, we term the inflation and
175 deflation phases as phase 1 (10:00–10:02) and 2 (10:02–10:20), respectively (Fig. 3).

176 The N–S component at KSS showed no significant change prior to 10:01 (Fig.

177 4b), suggesting a somewhat complex process during the initial stage of the inflation.
178 However, details of this tilt change were obscured by the following large tilt changes. We
179 therefore analyzed the tilt vectors of phases 1 and 2 (Fig. 4a).

180

181 **3.2 Modeling**

182 To determine the volume changes during the inflation (phase 1) and deflation
183 (phase 2), we modeled the deformation source causing the tilt changes. Although the tilt
184 vectors exhibit a simple radial pattern, the tilt change at N.KSHV was twice as large as
185 that recorded at N.KSYV, even though the two sites are located at a similar distance from
186 the center of the radial pattern (Fig. 4). The pattern of tilt change indicates the existence
187 of a subvertical crack rather than a simple point source. Furthermore, the new vent chain,
188 including MC, WC, and another smaller crater, formed over a distance of 450 m and
189 aligned along an azimuth of 112° (Figs 2d and 4). On the basis of these observations, we
190 propose that a subvertical tensile crack exists beneath the Kagaimike-kita PC.

191 We modeled a finite rectangular tensile crack in an elastic and homogeneous
192 half-space medium as proposed by Okada (1992). This model comprises the following

193 eight parameters: spatial location of the crack center (X, Y, and Z); horizontal length (L)
194 and vertical width (W) of the crack; crack azimuth (A) relative to north; dip angle (D)
195 relative to the ground surface; and dislocation (U) of the crack. Our model assumes
196 Lamé's constant $\lambda = \mu$ and $L/W = 2$. We searched for the best-fit combination of seven
197 parameters (X, Y, Z, L, A, D, and U) that produced the smallest misfit (root mean square
198 sum of the difference between the observed and calculated values of each tilt vector) by
199 the grid-search method.

200 We searched for the crack center (X, Y, and Z) within 500 m horizontally of the
201 MC and at 500–2100 m in elevation (0–1600 m asl) at intervals of 50 m. The horizontal
202 length of the crack (L) and dislocation were searched from 200 to 2400 m and 0.01 to
203 2.60 m, respectively. The search interval for L was 100 m, and for U was 0.01 m. The
204 crack azimuth (A) and dip angle (D) were searched from 70° to 160° and 15° to 165° ,
205 respectively, at intervals of 1° .

206

207 **3.3 Results**

208 Figure 5 compares the observed and modeled tilt vectors in phase 1. The N–S

209 component at JIE was excluded because of the absence of data at this site. The observed
210 tilt records are well fitted by a crack model with optimal parameters. The optimal location
211 of the center of the crack is located beneath the center of the MC at 1,000 m depth (1,100
212 m asl) with an azimuth (A) of 107° , which is consistent with the alignment of the MC
213 (112° ; Fig. 4). An optimal dip angle (D) of 88°N suggests the crack dips steeply to the
214 north. Such a subvertical crack can cause uplift on both its northern and southern sides.
215 Uplift of the northern side is consistent with the tilt changes recorded around YCL, while
216 uplift on the southern side can explain the large tilt change at N.KSHV relative to
217 N.KSYV. The optimal horizontal length (L), vertical width (W), and dislocation (U) are
218 1700 m, 850 m (assuming this is half of the horizontal length), and 0.35 m, respectively,
219 which resulted in a volumetric expansion of $\sim 5.1 \times 10^5 \text{ m}^3$.

220 Tilt vectors of phase 2 are in the opposite direction to those of phase 1, implying
221 contraction of the crack that expanded during phase 1. For simplicity, we assumed the
222 crack location, size, dip, and angle are fixed, and searched for the optimal dislocation in
223 phase 2. Figure 7 compares the observed and modeled tilt vectors in phase 2. The tilt
224 record at JIE was not used because there are no data after 10:02 due to an electrical

225 problem. Similar to the results for phase 1, the modeled tilt vectors are consistent with
226 the observations. The dislocation in phase 2 is estimated to be -0.25 m, implying a
227 deflation volume V_{Def} of $3.6 \times 10^5 \text{ m}^3$. Therefore, the net volume inflation V_{Net} during
228 the 2018 eruption was $1.5 \times 10^5 \text{ m}^3$.

229 To assess the uncertainty of our estimation of optimal crack location, Fig. 6
230 shows the spatial distribution of misfit values in horizontal and vertical cross-sections at
231 intervals of 100 m. For each panel in Fig. 6, we fixed Z (horizontal cross-section), X (N–
232 S cross-section), and Y (E–W cross-section) to optimum values of 1100 m asl,
233 36.629° (latitude), and 135.540° (longitude), respectively. Using the same method as in
234 section 3.2, we searched for the best-fit parameters L, A, D, U, and location (X and Y for
235 horizontal cross section, Y and Z for N–S cross-section, and X and Z for (E–W cross-
236 section) within the range described in section 3.2. If we accept a misfit of $<1 \mu\text{rad}$, the
237 central value of the uncertainty of the crack location is in the range of 600 m in the N–S
238 direction, 300 m in the E–W direction in the horizontal cross-section, and 500 m in the
239 vertical cross-sections (Fig. 6). The corresponding uncertainty in volume expansion is in
240 the range of 2.8×10^5 to $6.1 \times 10^5 \text{ m}^3$.

241 To assess the degree of uncertainty arising from the assumption in $L/W = 2$, we
242 searched for the best-fit combination of five parameters (Z , L , A , D , and U) using the
243 same method as above. The horizontal location of the crack center (X and Y) is fixed at
244 the MC, which corresponds to the optimal value obtained assuming $L/W = 2$. Figure S1
245 compares the observed and modeled tilt vectors in phase 1, assuming $L/W = 4$, 1, and 0.5.
246 In the cases given here, the center of the crack ranged between 400 and 1100 m asl. The
247 volumetric expansion is estimated to be 2.8×10^5 to 6.4×10^5 m³. Misfits were
248 minimized with the assumption of $L/W = 2$.

249

250 **4. Vapor release from the main crater**

251 **4.1 Volcanic ash cloud during the 2018 eruption**

252 Although vigorous tephra and gas emission occurred at the beginning of the
253 eruption (Fig. 2b), photographs (Fig. 2c), volcanic tremors, infrasound (Yamada et al.
254 2021), and tilt changes suggest that the eruption was brief. (i.e., ≤ 10 –15 min).
255 Surveillance video and photographs taken from the ground mostly focused on the eruption
256 site, and did not record the entire volcanic plume.

257 In such a situation, radar observations (Syarifuddin et al. 2019; Marzano et al.
258 2020) can track an ash cloud. Sato et al. (2018) presented a time-series of the ash cloud
259 echo of the phreatic eruption at Aso volcano on 8 October 2016. The echo obtained from
260 weather radar with a wavelength of 5.6 cm (C-Band), operated by the Japan
261 Meteorological Agency (JMA), is consistent with the distribution of the tephra deposit.
262 The total mass of ash ($3.2\text{--}7.5 \times 10^8$ kg), as estimated from the cloud height by the
263 echoes (12,000 m) and duration of ash emission (160–220 s), is consistent with field
264 observations ($6.0\text{--}6.5 \times 10^8$ kg; Sato et al. 2018).

265 During the 2018 MPCG eruption, C-Band weather radar stations of the JMA
266 clearly detected an echo of an ash cloud at a range of 0–9 km from the MC at 10:05–
267 10:10 (Meteorological Research Institute 2018). The track of the ash cloud echo coincides
268 with the distribution of the tephra deposit obtained by field geological surveys (Kametani
269 et al. submitted). The most distal position of the ash cloud was 9 km from MC at 10:05–
270 10:10, which implies a horizontal wind speed of ~20 m/s based on the onset time of the
271 eruption (10:02 JST). This estimate is consistent with speeds of 20–30 m/s recorded at
272 heights of 3,000–4,000 m asl at two sites (Fig. 1a) by radiosondes at 09:00. Therefore,

273 we estimated the change in height of the volcanic plume with distance from the MC (Fig.
274 7), based on reflectivity images from the Nagano radar (blue circle in Fig. 1a), located 66
275 km from Mt. Motoshirane. The ash cloud was detected at a range of 2,100–3,000 m asl
276 at 2 km from the MC. The ash cloud ascended with distance from the MC, reaching a
277 height of 3,100–5,400 m asl at 7 km from the MC.

278

279 **4.2 Simple plume model**

280 To evaluate the mass of water vapor emitted from the vents during the 2018
281 eruption M_v (kg), we used a simple model. Assuming a steady-state buoyant plume under
282 a constant horizontal wind, the height of a given position in the plume increases with
283 distance from the source to the power of 2/3 (Briggs 1969; Kagiya 1981):

284

$$285 \quad h = Cx^{\frac{2}{3}} \quad (1)$$

286

287 where h is the center of the height of the plume (m) and x is the distance from the source
288 (m). C can be estimated by least-squares fitting of the observed the center of the ash

289 height against the distance from the vent. Alternatively, C can be represented by an

290 empirical equation using horizontal wind velocity and heat discharge rate, as follows:

291

$$292 \quad C = 3.8 \times 10^{-5} u^{-1} \dot{q}^{\frac{1}{3}} \quad (2)$$

293

294 where u is horizontal wind speed (m/s) and \dot{q} is heat discharge rate (W).

295 We calculate plume height (h) as a function of distance from the MC (x)

296 assuming a heat discharge rate (\dot{q}) in the range of 0.1–100 GW under wind velocities (u)

297 of 20 and 30 km/s, respectively (Fig. 8). Equations (1) and (2) are consistent with the

298 empirical observation that a plume with strong buoyancy ascends rapidly, even in the case

299 of strong horizontal wind (Briggs 1969).

300 If a steady state plume is assumed for a duration of Δt , the total heat energy

301 emission Q_p (J) can be calculated by

302

$$303 \quad Q_p = \dot{q} \Delta t \quad (3)$$

304

305 Q_p is derived from the heat of vapor Q_v and volcanic ash Q_t :

306

$$307 \quad Q_p = Q_v + Q_t \quad (4)$$

308

309 Assuming that most of the vapor condenses near the vent and releases latent heat to the
310 plume, Q_v is calculated as the product of the total vapor mass M_v (in kg) and the specific
311 enthalpy H_v (kJ/kg) (Kagiyama et al. 1981; Terada and Sudo 2012; Narita et al. 2019):

312

$$313 \quad Q_v = H_v M_v \quad (5)$$

Formatted: Font color: Auto

314

315 We used an H_v value of 2,675 J/kg for vapor at 100°C with a pressure of $1 \times$
316 10^5 Pa (Wagner and Pruss 2002). The temperature of the volcanic plume is unknown, but
317 a high temperature (e.g., more than several hundred degrees Celsius) is unlikely, given
318 the main constituent minerals of volcanic ash emitted during the Motoshirane eruption
319 (Yaguchi et al., 2018). If the vapor temperature is 300°C, an H_v value of 3,074 kJ/kg
320 (Wagner and Pruss 2002) is used. We assume that the temperature dependence of H_v is

321 sufficiently small to ensure the validity of the discussion of water balance in Section 5.

322 Assuming that most of the heat of the tephra is converted to buoyancy near the vent, Q_t

323 can be calculated as

324

325 $Q_t = C_t T M_t$ (6)

Formatted: Font color: Auto

326

327 where C_t (J/kg/K) is the heat capacity averaged among the tephras, T (K) is the

328 temperature of the plume, and M_t (kg) is the total weight of ejecta. If H_v , C_t , and T are

329 known or given, then \dot{q} can be estimated from Equation (2), and if Δt is assumed, then

330 M_v can be calculated using the above equations.

331

332 4.3 Evaluation of water vapor emission from the vents

333 Equations (1) and (2) were used to obtain plume shapes for heat discharge rates.

334 C can be estimated by least-squares fitting of the plume track obtained by weather radar

335 (section 4.1; red bars in Fig. 8). Assuming wind speed u of 20 and 30 m/s on the basis of

336 measurements by radiosondes (red circles in Fig. 1a) at 09:00, the optimal heat discharge

337 rate is estimated to be 34 GW ($u = 20$ m/s) or 110 GW ($u = 30$ m/s). Considering the
338 uncertainty in wind speed, we evaluate the heat discharge rate \dot{q} to be 10–100 GW. This
339 value is >1000 times higher than the representative fumarolic heat discharge during non-
340 eruptive periods at active volcanoes in Japan (Kagiyama et al. 1981). Such a large heat
341 discharge of was estimated at Ontake volcano 24 hr after its 2014 eruption (Yamaoka et
342 al. 2016).

343 Assuming a duration for the emissions of 600 s, the total heat emission from
344 the plume Q_p is estimated to be $0.6\text{--}6.0 \times 10^{13}$ J (from Eq. 3). The total heat of the
345 volcanic ash Q_t is estimated to be 3×10^{12} J, which was calculated by multiplying $M_t =$
346 3×10^7 kg (Kametani et al. submitted) and a heat capacity of 1000 J/kg/K (i.e.,
347 representative of clay or volcanic rocks), with a temperature difference of 100°C relative
348 to ambient air. This leads to $Q_t = 3 \times 10^{12}$ J, which corresponds to 50% or 5% of Q_p .
349 Thus, the mass of vapor emission is estimated to be $0.1\text{--}2 \times 10^7$ kg, based on Eqs. (3)–
350 (6).

351

352 **5. Discussion**

353 During the 2018 MPCG eruption we detected a progressive ground deformation
354 by a borehole tiltmeter network. Although satellite synthetic aperture radar (SAR) is
355 useful for observing spatial surface deformation associated with a phreatic eruption (e.g.,
356 Kobayashi et al. 2018; Narita et al. 2020), a tiltmeter network with high temporal
357 resolution and dense spatial distribution provides details of progressive ground
358 deformation during an eruption (e.g., Ueda et al. 2013; Aloisi et al. 2019; Zobin et al.
359 2020). Our crack model implies that inflation of $5.1 \times 10^5 \text{ m}^3$ beneath the main crater
360 (MC) at Kagamike-kita PC for 2 min was followed by deflation of $3.6 \times 10^5 \text{ m}^3$. We did
361 not observe intense fumarolic activity or high-temperature volcanic gas emissions around
362 the MC after the eruption. The ejecta did not contain juvenile material (Yaguchi et al.
363 2019). Therefore, the rapid inflation/deflation was not caused by magma intrusion into
364 the crack, but was instead related to hydrothermal fluid. In this section, we discuss how
365 the eruption occurred, based on a conceptual model of the hydrothermal system beneath
366 Kusatsu–Shirane volcano.

367

368 **5.1 Conceptual model of the hydrothermal system at Kusatsu–Shirane volcano**

369 A self-sealed zone beneath volcanoes, formed by the precipitation of silica from
370 aqueous fluids (Saishu et al. 2014), can play a key role in constraining the pore pressure
371 of hydrothermal fluids (Fournier 1999). A self-sealed zone can be located at the brittle–
372 ductile (BD) transition zone, because relatively low-permeability silica precipitates
373 mainly at a temperature of 370–400°C, as inferred from data from deep wells, quartz
374 solubility calculations, and hydrothermal laboratory experiments (Fournier 1991, 1999;
375 Saishu et al. 2014). This narrow self-sealed zone separates the lithostatic pressure region
376 from the area where meteoric-derived hydrothermal fluids circulate through brittle crust
377 at hydrostatic pressures (Fig. 9). Such hydrothermal systems have been recognized based
378 on data including core and water samples from deep wells in geothermal fields, such as
379 at Kakkonda, Japan (Doi et al. 1998).

380 The bottom of a hypocenter distribution can delineate the BD transition zone,
381 because the hypocenter distribution of volcanic–tectonic earthquakes can mark the
382 boundary of quasistatic behavior (Fournier 1999; Ingebritsen and Manning 2010;
383 Castaldo et al. 2019). At Kusatsu–Shirane volcano, most hypocenters are located
384 shallower than 200 m asl (Figs 5–7), and events below sea level are extremely rare (Mori

385 et al. 2006; Tseng et al. 2020; Yamada et al., 2021). Therefore, we propose that a BD
386 transition zone exists at 200 m asl beneath Kusatsu–Shirane volcano (Fig. 9). Recent MT
387 surveys have detected a large and strong conductor between 500 m asl and 1000 m below
388 sea level (C2 of Matsunaga et al. 2020), which likely corresponds to a hydrothermal fluid
389 reservoir.

390 If a self-sealed BD transition zone episodically breaches, then sudden injection
391 of supercritical hydrothermal fluid at a lithostatic pressure to the region of hydrostatic
392 pressure may cause failure of the overlying brittle rock (Fournier 1999). The record of tilt
393 changes (Figs 5 and 7) suggests inflation of a subvertical crack extending from above the
394 BD transition zone to the surface, which provided a fluid pathway from depth.

395 The depth of a hydrothermal fluid reservoir associated with a phreatic eruption
396 can be a key control on the magnitude of a phreatic eruption (Stix and de Moor 2018).
397 On the basis of the crack model and MT resistivity structure, we consider the fluid
398 reservoir is located at 2 km depth beneath the MPCG (Figs 5 and 7). Compared with the
399 2018 MPCG eruption, the 2014 Ontake eruption produced an order of magnitude more
400 tephra (Maeno et al. 2016). Prior to the 2014 Ontake eruption, a tiltmeter and broadband

401 seismometer recorded rapid inflation of $1 \times 10^6 \text{ m}^3$ at a depth of 1,000 m, which was
402 likely caused by water boiling (Maeda et al. 2017). The hydrothermal fluid associated
403 with the 2014 Ontake eruption was derived from 3–6 km beneath the ground surface
404 (Kato et al. 2015; Narita et al. 2019), which is 2–4 km deeper than for the 2018 MPCG
405 eruption. Hydrothermal fluid from a deeper reservoir is likely to have a higher specific
406 enthalpy due to its closer proximity to magma, leading more explosive eruption.

407

408 **5.2 Deflation during phase 2**

409 Tilt changes recorded during phase 2 indicate deflation of $V_{Def} = 3.6 \times 10^5$
410 m^3 over a period of 10–20 min (Fig. 7). Assuming a density of 55.5 kg/m^3 , which is
411 representative of the vapor phase at the center of the crack at a hydrostatic pressure of 10
412 MPa (Wagner and Pruss, 2002), the corresponding mass is estimated to be $2 \times 10^7 \text{ kg}$,
413 which is comparable to the maximum mass estimate based on the plume track ($0.1\text{--}2 \times$
414 10^7 kg). However, the fluid volume in the crack can be larger than V_{Def} because of the
415 compressibility difference between hydrothermal fluid and surrounding rock (e.g.,
416 Rivalta and Segall 2008). Poroelasticity of the surrounding rock also affect the estimation

417 of the actual fluid volume (e.g., Juncu et al. 2019). Moreover, the fluid can be much
418 denser than assumed above, if the fluid is supercritical or a liquid phase. Given these
419 uncertainties, it is difficult to constrain the possible mass based on the deflation volume.
420 Therefore, the mass of 2×10^7 kg calculated above is a minimum estimate.

421 By comparing the mass M_v emitted as a plume and the minimum deflation mass
422 estimated from the deflation volume V_{Def} , we infer some of mass associated with the
423 deflation was dispersed underground (Fig. 9). We suggest that underground water acted
424 as a buffer against the impact of the sudden intrusion of hydrothermal fluid, which
425 absorbed the ascending hydrothermal fluid in the pre-existing crack. Gradual subsidence
426 around Kagamiike PC after the 2018 MPCG eruption (Himenatsu et al. 2020) was likely
427 caused by a relaxation of groundwater.

428 On 27 May 2011 (i.e., two months after the 2011 Mw 9.0 Tohoku Earthquake
429 located 300–600 km from Kusatsu–Shirane volcano; Ozawa et al. 2011), volcanic tremor
430 (Yamada et al., 2021) and rapid inflation followed by deflation (Fig. 10) were observed
431 at the MPCG, similar to the ground deformation associated with the 2018 Motoshirane
432 eruption. However, a phreatic eruption and unusual thermal activity did not occur in 2011.

433 The tilt vectors of the 2011 event (Fig. 10) are remarkably similar to those of the 2018
434 MPCG eruption (Fig. 4). Although only four tiltmeters were operating, we estimated the
435 volume changes during the inflation–deflation event in 2011 using the same crack as for
436 the 2018 MPCG eruption. As a result, we obtained an inflation of $5.8 \times 10^4 \text{ m}^3$ followed
437 by deflation of $1.4 \times 10^4 \text{ m}^3$. We consider that the subvertical crack opened but an eruption
438 failed to eventuate. Similar rapid inflation followed by deflation without eruption was
439 reported at Ontake volcano (Nakamichi et al. 2009) and Tokachidake volcano (Aoyama
440 et al. 2020). On the basis of the analysis of a VLP event in 2007, Nakamichi et al. (2009)
441 proposed that an enhanced flux of hot gases released from the magma heated a
442 hydrothermal system at 2000 m depth, which caused the vaporization of $8.8 \times 10^4 \text{ m}^3$ (1.75
443 $\times 10^6 \text{ kg}$) of water, followed by discharge of vapor from the crack.

444

445 **5.3 Heat associated with the 2018 eruption**

446 Kusatsu–Shirane volcano is one of the most active volcanoes in Japan in terms
447 of its persistent release of heat. To assess the impact of the 2018 eruption on the energy
448 budget of Kusatsu–Shirane volcano, we estimated the heat released by the 2018 eruption

449 and other thermal activity. The surface heat release from YCL is estimated to be 20 MW
450 (Ohba et al. 1994), corresponding to 6×10^{14} J/yr. The largest phreatic eruption in the
451 last 130 yr, which occurred during 1937–1939, produced heat of 5×10^{14} J, as calculated
452 from a tephra deposit of 5×10^9 kg (Minakami 1939) based on an assumption of a
453 temperature difference of 100 °C and a heat capacity of 1,000 J/kg/K.

454 During the 2018 eruption, the heat discharge associated with the plume is
455 estimated to have been $0.6\text{--}6.0 \times 10^{13}$ J (section 4). In addition, the tiltmeters suggest a
456 net volume increase V_{Net} after the eruption of 1.5×10^5 m³, which is large relative to
457 the heat release from the plume. Although the compressibility of the thermal fluid filling
458 the crack and surrounding rocks is unknown (Rivalta and Segall 2008), the deflation
459 volume V_{Def} provides a minimum estimate. Assuming the thermal fluid is at boiling
460 temperature at a pressure of 10 MPa, which corresponds to the center of the crack at 1 km
461 depth under hydrostatic pressure, the density and specific enthalpy of liquid water are 688
462 kg/m³ and 1,420 kJ/kg, respectively (Wagner and Pruss 2002). As such, V_{Net} is converted
463 to a minimum mass of 1.0×10^8 kg and minimum energy of 1.5×10^{14} J.

464 Although the atmospheric mass emission is small relative to past phreatic

465 eruptions at Kusatsu–Shirane volcano, the heat energy of the 2018 MPCG eruption is
466 comparable to or larger than the annual heat output of YCL or the largest eruption in the
467 past 130 yr. Therefore, the 2018 MPCG eruption is not negligible in terms of the energy
468 budget of Kusatsu–Shirane volcano.

469

470 **5.4 Implications for Kusatsu–Shirane volcano as a hazard risk**

471 Aligned small craters formed by past eruptions that are 10–30 m in horizontal
472 scale are found throughout the MPCG, suggesting that small phreatic eruptions have
473 occurred repeatedly (Ishizaki et al. 2020). These small craters are aligned NW–SE or
474 WNW–ESE, which is consistent with the crack azimuth (A) modeled in this study. The
475 direction of maximum compressive stress in this region is horizontal and oriented NW–
476 SE or WNW–ESE (Yoshida et al. 2012), allowing fluid to intrude from depth through a
477 crack with this orientation. We propose that the pre-existing crack has repeatedly acted
478 as a fluid pathway from the self-sealed BD transition zone to the surface for many years.
479 Indeed, similar rapid inflation ($5.8 \times 10^4 \text{ m}^3$) followed by deflation ($1.4 \times 10^4 \text{ m}^3$)
480 without a phreatic eruption was observed on 27 May 2011 (Fig. 10). The uncompensated

481 deflation volume can be dispersed or absorbed by surrounding low-enthalpy underground
482 water, which acts as a buffer and suppresses explosions. We infer that the inflation of
483 hydrothermal fluid in the crack in 2011 was too small to breach the surface rocks above
484 the crack.

485 Yamada et al. (2021) reported that the source location of the volcanic tremor
486 that occurred prior to the eruption was the eastern side of APC (Fig. 1), 1 km north of the
487 MC on Kagamiike-kita PC. The volcanic tremor was likely caused by small shear
488 fractures induced by a sudden intrusion of fluid (Yamada et al. 2021). The tilt vector of
489 KSS before 10:01 (Fig. 4b) suggests a pressure source close to the tremor source near
490 APC. We suspect that two cracks, beneath the eastern side of APC and beneath
491 Kagamiike-kita PC, were opened at the same time, but an eruption of APC failed to
492 eventuate.

493 Aligned small craters associated with past small phreatic eruptions are common
494 at Kusatsu–Shirane volcano (Ishizaki et al. 2020), but have been rarely documented and
495 monitored, particularly at the MPCG. Therefore, these events pose a future risk to nearby
496 tourists visiting the area.

497

498 **5.5 Relationship between the MPCG and SPCG**

499 From March 2014 to 2016, the SPCG experienced a microearthquake swarm,
500 ground deformation indicating an increase in volume of $1.2 \times 10^5 \text{ m}^3$ over 20 months
501 (Fig. S2), an increase in the Cl and SO₄ concentration of YCL, and an increase in the
502 CO₂/H₂S ratio of nearby fumaroles (SPCG unrest in 2014) (Ohba et al. 2019b). Moreover,
503 three months after the 2018 MPCG eruption, a shallow inflation and a marked increase
504 in seismicity occurred at SPCG from April 2018 (MPCG-SPCG unrest in 2018). There is
505 no clear evidence of dike intrusion at shallow depths, but GNSS measurements have
506 shown that a sill-like source located a few kilometers northwest of the SPCG at a depth
507 of 5 km was inflated during 2014–2016 and 2018–2020 (Munekane, submitter to this
508 special issue). The periods of inflations coincide with the period of SPCG unrest in 2014
509 and MPCG–SPCG unrest in 2018. These findings suggest that the supply of magmatic
510 fluid from the sill-like source to shallow depths enhanced the volcanic activity of
511 Kusatsu–Shirane volcano (Munekane, submitter to this special issue).

512 A large fluid reservoir (C2 conductive zone) underlies the region beneath the

513 MPCG and SPCG (Matsunaga et al. 2020), suggesting that magmatic fluid supply to the
514 C2 conductive zone can affect the activity of the MPCG as well as the SPCG. Tilt records
515 have revealed a subvertical crack extending from the C2 conductive zone to the surface
516 (Figs. 5 and 8); therefore, we propose that the hydrothermal fluid that was supplied from
517 the sill-like source triggered the 2018 MPCG eruption, which highlights the classification
518 of Kusatsu–Shirane volcano as a “persistently restless volcano” (Roman et al. 2019) or
519 “volcano with slow unrest” (Stix 2018).

520 One possible mechanism for the triggering of the 2018 MPCG eruption is self-
521 sealing of the fluid pathway to the SPCG during the unrest. Temporary sealing prior to a
522 phreatic eruption has been reported for many volcanoes (Christenson et al. 2011; Geirsson
523 et al. 2014; Ohba et al. 2019a; de Moor et al. 2019). It is plausible that the fluid pathway
524 to the SPCG was sealed during the period of quiescence after SPCG unrest in 2014,
525 leading to the eruption at the MPCG in 2018 in response to the increase in magmatic fluid
526 supplied from depth.

527 Three months after the 2018 MPCG eruption, the SPCG underwent shallow
528 inflation and a marked increase in seismicity. Fumarolic activity and seismicity in the

529 MPCG showed a decline after the eruption, while the sill-like source inflation continued,
530 indicating that the fluid path to the MPCG had been tightly sealed after the eruption.
531 However, there are no observations to suggest the mechanism or physicochemical process
532 of this sealing. Sealing is one possible scenario, but further observations, such as defining
533 the subsurface structure and monitoring the C2 conductor, will be necessary to more fully
534 understand the conditions that determine whether an eruption occurs, as well as the
535 possible location of a phreatic eruption.

536

537 **6. Conclusions**

538 A tiltmeter network recorded rapid inflation followed by deflation during a
539 phreatic eruption in 2018 at the MPCG. The tilt records can be explained by a subvertical
540 crack model centered at 1,100 m asl beneath the new crater. The crack azimuth is
541 consistent with the direction of chains of small craters formed by past eruptions and the
542 orientation of maximum compressive stress in the region, allowing fluid to intrude from
543 depth through the crack. The inflation and deflation volumes associated with the 2018
544 MPCG eruption are estimated to be 5.1×10^5 and $3.6 \times 10^5 \text{ m}^3$, respectively, meaning

545 that $1.5 \times 10^5 \text{ m}^3$ of expanded volume remained underground. We estimated the
546 discharged water mass in the volcanic plume to be $0.1\text{--}2.0 \times 10^7 \text{ kg}$, which is smaller
547 than the mass associated with the deflation. We propose that underground water acted as
548 a buffer against the sudden injection of hydrothermal fluid, which absorbed some of the
549 hydrothermal fluid ascending through the crack. Gradual subsidence around the
550 Kagamiike PC after the 2018 MPCG eruption inferred from SAR was likely caused by a
551 relaxation of intruded groundwater at shallow depths. This is the second time that rapid
552 inflation followed by deflation has occurred at Kusatsu–Shirane volcano since the first
553 tiltmeter was established there in 1991. We suggest that similar small phreatic or failed
554 eruptions affected by groundwater have repeatedly occurred in the MPCG. Although the
555 ejecta mass of the 2018 phreatic eruption is small, the total heat associated with the
556 ground deformation is estimated to be $\geq 10^{14} \text{ J}$, which is comparable with or exceeds the
557 estimated annual heat release from YCL and that from the largest eruption during the past
558 130 yr. Therefore, the 2018 MPCG eruption was not negligible in terms of the energy
559 budget of Kusatsu–Shirane volcano. Prior to the 2018 eruption, precursors of the eruption
560 were not observed at MPCG. However, the SPCG had exhibited volcanic unrest since

561 2014. We propose that enhanced amounts of magmatic fluid supplied from depth into the
562 hydrothermal reservoir 2 km beneath the MPCG and SPCG opened a pre-existing
563 subvertical crack between the reservoir and ground surface, causing the 2018 MPCG
564 eruption.

565

566 **Declarations**

567 **Ethics approval and consent to participate**

568 Not applicable.

569

570 **Consent for publication**

571 Not applicable.

572

573 **List of abbreviations**

574 APC = Ainomine Pyroclastic Cone

575 asl = Above sea level

576 BD = Brittle–ductile

577 HF = High frequency

578 JMA = Japan Meteorological Agency

579 JST = Japan Standard Time

580 KSVO = Kusatsu–Shirane Volcano Observatory, Tokyo Institute of Technology

581 MC, WC, SC = Main, west, and south Crater of the 2018 eruption

582 MPCG = Motoshirane Pyroclastic Cone Group

583 MT = Magnetotelluric

584 NIED = National Research Institute for Earth Science and Disaster Resilience

585 PC = Pyroclastic cone

586 SAR = Synthetic aperture radar

587 SPCG = Shirane Pyroclastic Cone Group

588 YCL= Yugama Crater Lake

589

590 **Availability of data and materials**

591 Tilt data from KSVO are available from the corresponding author on reasonable

592 request. Tilt data from NIED and JMA can be downloaded from

593 <https://www.vnet.bosai.go.jp>.

594

595 **Competing interests**

596 The authors declare that they have no competing interests.

597

598 **Funding**

599 This study was supported by the Ministry of Education, Culture, Sports, Science and
600 Technology (MEXT) of Japan, under its Earthquake and Volcano Hazards Observation
601 and Research Program, the Integrated Program for Next Generation Volcano Research
602 and Human Resource Development and Grant-in-Aid for scientific research (No.
603 17K20141).

604

605 **Authors' contributions**

606 AT constructed the crack model, estimated water discharge, and drafted the manuscript.
607 WK, YO, TY, MY, and SO helped to interpret the results of analyses through discussions.
608 TO, HA, and TT assisted the observation and helped to improve the manuscript. All
609 authors read and approved the final manuscript.

610

611 **Acknowledgements**

612 We thank the National Research Institute for Earth Science and Disaster Resilience
613 (NIED) for sharing the tilt records of N.KSHV, N.KSYV, and N.KSNV. The Japan
614 Meteorological Agency provided the tilt records from V.KSAO for the event in 2011. The

615 town of Kusatsu, Agatsuma District Forest Office, Ministry of Agriculture, Forestry and
616 Fisheries, and Ministry of Environment provided the approval for our observations. We
617 are grateful to the Kusatsu Tourism Cooperation for allowing us to use photographs. An
618 early version of the tiltmeter network at Kusatsu–Shirane volcano was established by
619 Jun’ichi Hirabayashi in the 1990s. We thank two anonymous reviewers for their valuable
620 comments. Some figures were drawn with Generic Mapping Tools (Wessel and Smith
621 1998). We used a 10 m mesh digital elevation model from the Geospatial Information
622 Authority of Japan (GSI) to draw the topographic maps

623

624 **Authors' information**

625 1 Volcanic Fluid Research Center, School of Science, Tokyo Institute of Technology,
626 2-12-1 Ookayama, Meguro, Tokyo 152-8551, Japan. 2 Sakurajima Volcano
627 Research Center, Disaster Prevention Research Institute, Kyoto University, 1722-19
628 Sakurajima-Yokoyama, Kagoshima 891-1419, Japan. 3 Graduate School of
629 Science, Tohoku University, 6-6, Aramaki-aza-Aoba, Aoba-ku, Sendai 980-8578,
630 Japan. 4 Aso Volcanological Laboratory, Kyoto University, 5280 Kawayo,

631 Minami-Aso, Kumamoto 869-1404, Japan. 5 Institute of Seismology and
632 Volcanology, Faculty of Science, Hokkaido University, N10W8, Kita-ku, Sapporo,
633 Hokkaido 060-0810, Japan. 6 Volcanology Research Department, Meteorological
634 Research Institute, Japan Meteorological Agency, 1-1 Nagamine, Tsukuba, Ibaraki 305-
635 0052, Japan

636

637 **Endnotes**

638 Not applicable.

639

640 **References**

641 Aoyama H, Tanaka R, Hashimoto T, Murakami M, Narita S (2020) Seismic and
642 geodetic monitoring near the active crater at Tokachidake volcano (preliminary
643 report). Geophysical Bulletin of Hokkaido University 83:25-48.
644 doi:10.14943/gbhu.83.25

645 Aloisi M, Bonaccorso A, Cannavò F, Currenti G, Gambino S (2020) The 24 December
646 2018 eruptive intrusion at Etna volcano as revealed by multidisciplinary

647 continuous deformation networks (CGPS, borehole strainmeters and tiltmeters). J
648 Geophys Res Solid Earth 125:e2019JB019117.
649 <https://doi.org/10.1029/2019JB019117>

650 Barberi F, Bertagnini A, Landi P, Principe C (1992) A review on phreatic eruptions and
651 their precursors. J Volcanol Geotherm Res 52:231–246.
652 [https://doi.org/10.1016/0377-0273\(92\)90046-G](https://doi.org/10.1016/0377-0273(92)90046-G)

653 Briggs GA (1969) Plume Rise. Critical Review Series, Rep. TID-25075, Atomic Energy
654 Commission, Washington, DC, USA

655 Castaldo R, D'Auria L, Pepe S, Solaro G, Novellis VD, Tizzani P (2019) The impact of
656 crustal rheology on natural seismicity: Campi Flegrei caldera case study.
657 Geoscience Frontiers 10:453-466. <https://doi.org/10.1016/j.gsf.2018.02.003>.

658 Christenson BW, Reyes AG, Young R, Moebis A, Sherburn S, Cole - Baker J, Britten
659 K (2010) Cyclic processes and factors leading to phreatic eruption events: Insights
660 from the 25 September 2007 eruption through Ruapehu Crater Lake, New Zealand.
661 J Volcanol Geotherm Res 191:15–32.
662 <https://doi.org/10.1016/j.jvolgeores.2010.01.008>

663 de Moor JM, Stix J, Avarad G, Muller C, Corrales E, Diaz JA, Alan A, Brenes J,
664 Pacheco J, Aiuppa A, Fischer TP (2019) Insights on hydrothermal - magmatic
665 interactions and eruptive processes at Poás volcano (Costa Rica) from high -
666 frequency gas monitoring and drone measurements. *Geophys Res Lett* 46:1293–
667 1302. <https://doi.org/10.1029/2018GL080301>

668 Doi N, Kato O, Ikeuchi K, Komatsu R, Miyazaki S, Akaku K, Uchida T (1998) Genesis
669 of the plutonic-hydrothermal system around quaternary granite in the Kakkonda
670 geothermal system, Japan. *Geothermics* 27: 663–690.
671 [https://doi.org/10.1016/S0375-6505\(98\)00039-X](https://doi.org/10.1016/S0375-6505(98)00039-X)

672 Fournier RO (1991) The transition from hydrostatic to greater than hydrostatic fluid
673 pressure in presently active continental hydrothermal systems in crystalline rock.
674 *Geophys Res Lett* 18:955–958. <https://doi.org/10.1029/91GL00966>

675 Fournier RO (1999) Hydrothermal Processes related to movement of fluid from plastic
676 into brittle rock in the magmatic–epithermal environment. *Econ Geol* 94:1193–
677 1211. <https://doi.org/10.2113/gsecongeo.94.8.1193>

678 Geirsson H, Rodgers M, LaFemina P, Witter M, Roman D, Muñoz A, Tenorio V,

679 Alvarez J, Jacobo VC, Nilsson D, Galle B, Feineman MD, Furman T, Morales A
680 (2014) Multidisciplinary observations of the 2011 explosive eruption of Telica
681 volcano, Nicaragua: Implications for the dynamics of low-explosivity ash
682 eruptions. *J Volcanol Geotherm Res* 271:55-69.
683 <https://doi.org/10.1016/j.jvolgeores.2013.11.009>

684 Himematsu Y, Ozawa T, Aoki Y (2020) Coeruptive crustal deformation associated with
685 the 2018 Kusatsu-Shirane phreatic eruption based on PALSAR-2 time-series
686 analysis. *Earth Planets Space* 72:116. <https://doi.org/10.1186/s40623-020-01247-6>

687 Ingebritsen SE, Manning CE (2010) Permeability of the continental crust: dynamic
688 variations inferred from seismicity and metamorphism. *Geofluids*, 10, 193–205.
689 <https://doi.org/10.1111/j.1468-8123.2010.00278.x>

690 Ishizaki Y, Nigorikawa A, Kametani N, Yoshimoto M, Terada A (2020) Geology and
691 eruption history of the Motoshirane Pyroclastic Cone Group, Kusatsu-Shirane
692 Volcano, central Japan. *J Geol Soc Japan* 126:473–491.
693 <https://doi.org/10.5575/geosoc.2020.0022> **(in Japanese with English Abstract)**

694 Juncu D, Árnadóttir Th, Geirsson H, Gunnarsson G (2019) The effect of fluid

695 compressibility and elastic rock properties on deformation of geothermal
696 reservoirs, *Geophys Int J* 217:122-134. <https://doi.org/10.1093/gji/ggz011>

697 Kagiya T (1981) Evaluation methods of heat discharge and their applications to the
698 major active volcanoes in Japan. *J Volcanol Geotherm Res* 9: 87–97.
699 [https://doi.org/10.1016/0377-0273\(81\)90016-0](https://doi.org/10.1016/0377-0273(81)90016-0)

700 Kametani N, Ishizaki Y, Yoshimoto M, Maeno F, Terada A, Furukawa R, Honda R,
701 Ishizuka Y, Komori J, Nagai M, Takarada S, Total mass estimate of the January
702 23, 2018 phreatic eruption of the Kusatsu-Shirane Volcano, central Japan. *Earth
703 Planets Space* (submitted to this issue)

704 Kato A, Terakawa T, Yamanaka Y, Maeda Y, Horikawa S, Matsuhira K, Okuda T
705 (2015) Preparatory and precursory processes leading up to the 2014 phreatic
706 eruption of Mount Ontake, Japan. *Earth Planets Space* 67:111.
707 <https://doi.org/10.1186/s40623-015-0288-x>

708 Kobayashi T, Morishita Y, Munekane H (2018) First detection of precursory ground
709 inflation of a small phreatic eruption by InSAR. *Earth Planet Sci Lett* 491: 244–254.
710 <https://doi.org/10.1016/j.epsl.2018.03.041>

711 Maeda Y, Kato A, Yamanaka Y (2017) Modeling the dynamics of a phreatic eruption
712 based on a tilt observation: Barrier breakage leading to the 2014 eruption of Mount
713 Ontake, Japan. *J Geophys Res Solid Earth* 122: 1007–1024.
714 <https://doi.org/10.1002/2016JB013739>

715 Maeno F, Nakada S, Oikawa T, Yoshimoto M, Komori J, Ishizuka Y, Takeshita Y,
716 Shimano T, Kaneko T, Nagai M (2016) Reconstruction of a phreatic eruption on
717 27 September 2014 at Ontake Central Japan, based on proximal pyroclastic density
718 current and fallout deposits. *Earth Planets Space* 68:82.
719 <https://doi.org/10.1186/s40623-016-0449-6>

720 Marzano FS, Mereu L, Scollo S, Donnadieu F, Bonadonna C (2020) Tephra mass
721 eruption rate from ground-based X-Band and L-Band microwave radars during the
722 November 23, 2013, Etna paroxysm. *IEEE Transactions on Geoscience and*
723 *Remote Sensing* 58: 3314-3327. doi:10.1109/TGRS.2019.2953167

724 Matsunaga Y, Kanda W, Takakura S, Koyama T, Saito Z, Seki K, Suzuki A, Kishita T,
725 Kinoshita Y, Ogawa Y (2020) Magmatic hydrothermal system inferred from the
726 resistivity structure of Kusatsu–Shirane Volcano. *J Volcanol Geotherm Res*

727 390:106742. <https://doi.org/10.1016/j.jvolgeores.2019.106742>

728 Meteorological Research Institute JMA (2018) Eruption cloud echoes from Mt.

729 Kusatsu-Shirane on January 23rd, 2018, observed by JMA weather radars. Reports

730 of Coordinating Committee for Prediction of Volcanic Eruption 129: 78-82.

731 <https://www.data.jma.go.jp/svd/vois/data/tokyo/STOCK/kaisetsu/CCPVE/Report/1>

732 [29/kaiho_129_08.pdf](https://www.data.jma.go.jp/svd/vois/data/tokyo/STOCK/kaisetsu/CCPVE/Report/1) (**in Japanese**)

733 Minakami T (1939) Explosive activities of volcano Kusatsu-Shirane during 1937 and

734 1938. Bull Earthq Res Inst 17:590–623. <http://hdl.handle.net/2261/10454>

735 Mori T, Hirabayashi J, Nogami K, Onizawa S (2006) A new seismic observation system

736 at the Kusatsu-Shirane volcano. Bull Volcanol Soc Japan 53:41–47.

737 https://doi.org/10.18940/kazan.51.1_41 (**in Japanese with English abstract**)

738 Munekane H, Modeling long-term volcanic deformation at the Kusatsu-Shirane and

739 Asama volcanoes, Japan using the GNSS coordinate time series. Earth Planets

740 Space (submitted to this special issue)

741 Nakamichi H, Kumagai H, Nakano M, Okubo M, Kimata F, Ito Y, Obara K (2009)

742 Source mechanism of a very-long-period event at Mt Ontake, central Japan:

743 response of a hydrothermal system to magma intrusion beneath the summit. J
744 Volcanol Geotherm Res 187:167–177.
745 <https://doi.org/10.1016/j.jvolgeores.2009.09.006>

746 Narita S, Murakami M, Tanaka R (2019) Quantitative relationship between plume
747 emission and multiple deflations after the 2014 phreatic eruption at Ontake
748 volcano, Japan. Earth Planets Space 71:145. [https://doi.org/10.1186/s40623-019-](https://doi.org/10.1186/s40623-019-1124-5)
749 1124-5

750 Narita, S, Ozawa T, Aoki Y, Shimada M, Furuya M, Takada Y, Murakami M (2020)
751 Precursory ground deformation of the 2018 phreatic eruption on Iwo-Yama volcano,
752 revealed by four-dimensional joint analysis of airborne and spaceborne InSAR. Earth
753 Planets Space 72:145. <https://doi.org/10.1186/s40623-020-01280-5>

754 Nurhasan, Ogawa Y, Ujihara N, Tank SB, Honkura Y, Onizawa S, Mori T, Makino M
755 (2006) Two electrical conductors beneath Kusatsu-Shirane volcano, Japan,
756 imaging by audiomagnetotellurics and their implications for hydrothermal system.
757 Earth Planet Space 58:1053–1059. <https://doi.org/10.1186/BF03352610>

758 Ogawa Y, Aoyama H, Yamamoto M, Tsutsui T, Terada A, Ohkura T, Kanda W,

759 Koyama T, Kaneko T, Ominato T, Ishizaki Y, Yoshimoto M, Ishimine Y, Nogami
760 K, Mori T, Kikawada Y, Kataoka K, Matsumoto T, Kamiisi I, Yamaguchi S, Ito Y,
761 Tsunematsu K (2018) Comprehensive survey of 2018 Kusatsu-Shirane Eruption.
762 Proc Symp on the Natural Disaster Sciences 55:25–30 (**in Japanese**)

763 Ohba T, Hirabayashi J, Nogami K (1994) Water, heat and chloride budgets of the crater
764 lake Yugama at Kusatsu-Shirane volcano, Japan. *Geochem J* 28:217–231.
765 <https://doi.org/10.2343/geochemj.28.217>

766 Ohba T, Hirabayashi J, Nogami K (2008) Temporal changes in the chemistry of lake
767 water within Yugama Crater, Kusatsu-Shirane volcano, Japan: implications for the
768 evolution of the magmatic hydrothermal system. *J Volcanol Geotherm Res*
769 178:131–144. <https://doi.org/10.1016/j.jvolgeores.2008.06.015>

770 Ohba T, Yaguchi M, Nishino K, Numanami N, Daita Y, Sukigara C, Ito M, Tsunogai U
771 (2019a) Time variations in the chemical and isotopic composition of fumarolic
772 gases at Hakone volcano, Honshu Island, Japan, over the earthquake swarm and
773 eruption in 2015, interpreted by magma sealing model. *Earth Planets Space* 71:48
774 <https://doi.org/10.1186/s40623-019-1027-5>

775 Ohba T, Yaguchi M, Nishino K, Numanami N, Tsunogai U, Ito M, Shingubara R
776 (2019b) Time variation in the chemical and isotopic composition of fumarolic
777 gasses at Kusatsu–Shirane Volcano, Japan. *Front Earth Sci* 7:249.
778 <https://doi.org/10.3389/feart.2019.00249>

779 Okada, Y. (1992) Internal deformation due to shear and tensile faults in a half-space.
780 *Bull Seism Soc Am* 82:1018-1040

781 Ozawa S, Nishimura T, Suito H, Kobayashi T, Tobita M, Imakiire T (2011) Coseismic
782 and postseismic slip of the 2011 magnitude-9 Tohoku-Oki earthquake. *Nature*
783 475:373–376. <https://doi.org/10.1038/nature10227>

784 Rivalta E, Segall P (2008) Magma compressibility and the missing source for some dike
785 intrusions. *Geophys Res Lett* 35:L04306. <https://doi.org/10.1029/2007GL032521>

786 Roman DC, LaFemina PC, Bussard R, Stephens K, Wauthier C, Higgins M, Feineman
787 M, Arellano S, de Moor JM, Avaró G, Cruz MM, Burton M, Varnam M, Saballos
788 A, Ibarra M, Strauch W, Tenorio V (2019) Mechanisms of unrest and eruption at
789 persistently restless volcanoes: Insights from the 2015 eruption of Telica Volcano,
790 Nicaragua. *Geochem Geophys Geosys* 20: 4162–4183.

791 <https://doi.org/10.1029/2019GC008450>

792 Saishu H, Okamoto A, Tsuchiya, N. (2014) The significance of silica precipitation on
793 the formation of the permeable–impermeable boundary within Earth’s crust. *Terra*
794 *Nova* 26:253–259. <https://doi.org/10.1111/ter.12093>

795 Sato E, Fukui K, Shimbori T (2018) Aso volcano eruption on October 8, 2016, observed
796 by weather radars. *Earth Planets Space* 70:105. [https://doi.org/10.1186/s40623-](https://doi.org/10.1186/s40623-018-0879-4)
797 [018-0879-4](https://doi.org/10.1186/s40623-018-0879-4)

798 Sato H, Takahashi H, Yamamoto E, Fukuo N, Uehara M, Terasawa Y (1980)
799 Development of the crustal tilt observation method using borehole-type tiltmeters.
800 *Jisin* 33:343-368. https://doi.org/10.4294/zisin1948.33.3_343

801 Stix J (2018) Understanding fast and slow unrest at volcanoes and implications for
802 eruption forecasting. *Front Earth Sci* 6:56.
803 <https://doi.org/10.3389/feart.2018.00056>

804 Stix J and de Moor JM (2018) Understanding and forecasting phreatic eruptions driven
805 by magmatic degassing. *Earth Planets Space* 70:83.
806 <https://doi.org/10.1186/s40623-018-0855-z>

807 Syarifuddin M, Oishi S, Hapsari RI, Shiokawa J, Mawandha HG, Iguchi M (2019)
808 Ground observation of tephra particles: On the use of weather radar for estimating
809 volcanic ash distribution, *J Disaster Res* 14:151-159.
810 <https://doi.org/10.20965/jdr.2019.p0135>

811 Tanada T, Ueda H, Nagai M, Ukawa M (2017) NIED's V-net, the fundamental volcano
812 observation network in Japan, *J Disaster Res* 12: 926-931.
813 <https://doi.org/10.20965/jdr.2017.p0926>

814 Terada A, Sudo Y (2012) Thermal activity within the western-slope geothermal zone of
815 Aso volcano, Japan: Development of a new thermal area. *Geothermics* 42: 56-64,
816 <https://doi.org/10.1016/j.geothermics.2012.01.003>.

817 Terada A, Hashimoto T (2017) Variety and sustainability of volcanic lakes: response to
818 subaqueous thermal activity predicted by a numerical model. *J Geophys Res Solid*
819 *Earth* 122:6108–6130. <https://doi.org/10.1002/2017JB014387>

820 Terada A (2018) Kusatsu-Shirane volcano as a site of phreatic eruptions. *Jour Geol Soc*
821 *Japan* 124:251–270. <https://doi.org/10.5575/geosoc.2017.0060> (**in Japanese and**
822 **English abstract**)

823 Tseng KH, Ogawa Y, Nurhasan, Tank SB, Ujihara N, Honkura Y, Terada A, Usui Y,
824 Kanda W (2020) Anatomy of active volcanic edifice at the Kusatsu–Shirane
825 volcano, Japan, by magnetotellurics: hydrothermal implications for volcanic
826 unrests, *Earth Planet Space* 72:161. <https://doi.org/10.1186/s40623-020-01283-2>
827 Ueda H, Kozono T, Fujita E, Kohno Y, Nagai M, Miyagi Y, Tanada T (2013) Crustal
828 deformation associated with the 2011 Shinmoe-dake eruption as observed by
829 tiltmeters and GPS. *Earth Planet Space* 65:4.
830 <https://doi.org/10.5047/eps.2013.03.001>
831 Wagner W, Pruss A (2002) The IAPWS formulation 1995 for the thermodynamic
832 properties of ordinary water substance for general and scientific use. *J Phys Chem*
833 *Ref Data* 31:387–535. <https://doi.org/10.1063/1.1461829>
834 Wessel P, Smith WHF (1998) New, improved version of generic mapping tools
835 released. *EOS Trans AGU* 79:579. <https://doi.org/10.1029/98EO00426>
836 Yaguchi M, Ohba T, Numanami N, Kawaguchi R (2019) Constituent mineral and
837 water-soluble components of volcanic ash from the 2018 eruption of Mt.
838 Motoshirane of Kusatsu-Shirane Volcano, Japan. *J Disaster Res* 14:991–995.

839 <https://doi.org/10.20965/jdr.2019.p0991>

840 Yamada T, Kurokawa AK, Terada A, Kanda W, Ueda H, Aoyama H, Ohkura T, Ogawa
841 Y, Tanada T (2021) Locating hydrothermal fluid injection of the 2018 phreatic
842 eruption at Kusatsu-Shirane volcano with volcanic tremor amplitude. *Earth Planet
843 Space* 73:14. <https://doi.org/10.1186/s40623-020-01349-1>

844 Yamamoto M, Aoyama H, Tsutsui T, Terada A, Kanada W, Ogawa Y (2018)
845 Temporary seismic observation at Kusatsu-Shirane volcano, Japan. Abstracts of
846 Japan Geoscience Union Meeting 2018 SVC41-P10.

847 Yamaoka K, Geshi N, Hashimoto T, Ingebritsen SE, Oikawa T (2016) Special issue “The
848 phreatic eruption of Mt. Ontake volcano in 2014”. *Earth Planets Space* 68:175.
849 <https://doi.org/10.1186/s40623-016-0548-4>

850 Yoshida K, Hasegawa A, Okada T, Iinuma T, Ito Y, Asano Y (2012) Stress before and
851 after the 2011 great Tohoku - oki earthquake and induced earthquakes in inland
852 areas of eastern Japan. *Geophys Res Lett* 39: L03302.
853 <https://doi.org/10.1029/2011GL049729>.

854 Zobin VM, Bretón M, Ramírez JJ, Santiago H (2020) Transition from passive to pre-

855 extrusion degassing of ascending andesitic magma before the lava dome-building
856 eruption as derived from the seismic signals and tilt changes: Volcán de Colima,
857 México, August–September 2004. *J Volcanol Geotherm Res* 401:106971.
858 <https://doi.org/10.1016/j.jvolgeores.2020.106971>.
859

860 **Table 1 Details of the instruments in the tiltmeter network**

861

862 **Fig. 1** Location and topography of Kusatsu–Shirane volcano. **a** Location map of Kusatsu–

863 Shirane volcano in Japan (star). Blue and red circles represent the locations of the Nagano

864 weather radar site and an aerological observatory using a balloon and radiosonde,

865 respectively (both operated by the Japan Meteorological Agency). **b** Topographic map of

866 Kusatsu–Shirane volcano. Solid lines are topographic contours at intervals of 30 m. Red

867 squares and circles indicate the locations of tiltmeters installed at the bottom of boreholes

868 and at a depth of 1–2 m from the ground surface, respectively (Table 1). Yellow squares

869 (MC, WC, and SC) indicate the locations of craters that formed during the 2018 eruption.

870 PC = pyroclastic cone; MPCG = Motoshirane Pyroclastic Cone Group; SPCG = Shirane

871 Pyroclastic Cone Group; YCL = Yugama Crater Lake; MC = main crater; WC = west

872 crater; SC = south crater.

873

874 **Fig. 2 a** Aerial photograph of Kusatsu–Shirane volcano (taken on 5 November 2015). PC

875 = pyroclastic cone; MPCG = Motoshirane Pyroclastic Cone Group; SPCG = Shirane

876 Pyroclastic Cone Group; YCL = Yugama Crater Lake. **b** Eruption cloud and ballistic
877 block falls hitting the ski slope, (photograph taken by the Kusatsu Tourism Cooperation
878 at 10:02 JST on 23 January 2018). **c** Weak volcanic cloud rising from Kagamiike-kita PC
879 at about 10:20 JST on 23 January 2018. **d** Aerial photograph of the new main crater (MC)
880 at Kagamiike-kita PC and south crater (SC) at Kagamiike PC formed during the 2018
881 eruption (photograph taken on 25 June 2018). The west crater (WC) is outside the
882 photograph.

883

884 **Fig. 3** Tilt components recorded at 09:50–10:10 (JST) on 23 January 2018. **a** North–south
885 and **b** west–east components. Acausal low-pass filters with cut-off frequencies of 0.034
886 and 0.021 Hz were applied to the tilt records of JTS-33 (KSE, KSS, KSW, N.KSHV,
887 N.KSYV, and N.KSNV) and 701-2A (YNW and JIE), respectively. **c** Raw vertical
888 ground velocity waveform at KSS. See Fig. 1 and Table 1 for station names and locations.
889 We term the inflation and deflation phases as phase 1 and phase 2, respectively. The time
890 of eruption onset was estimated by Yamada et al. (2021).

891

892

893 **Fig. 4** Tilt vectors in the study area. Yellow rectangles show the localities of vents formed
894 during the 2018 eruption. White, red, and gray circles represent hypocenters for the
895 periods from 1 January 2016 to 22 January 2018 (before the eruption), from 23 January
896 to 22 April 2018 (after the eruption), and from 22 to 23 April 2018 (representative of
897 SPCG unrest in 2018), respectively, as determined by the Kusatsu-Shirane Volcano
898 Observatory, Volcano Fluid Research Center, Tokyo Institute of Technology. **a** Phase 1
899 (black arrows, Fig.3) and phase 2 (white arrows, Fig.3). **b** First half of phase 1 (black
900 arrows; 10:00–10:01 JST). Note that the vector scale is different from that in Fig. 4a.

901

902 **Fig. 5** Comparison of observed (red arrows) and modeled (blue arrows) tilt vectors of
903 phase 1 (Fig. 3). The location of the modeled crack is represented by the yellow rectangle.
904 Modeled vertical displacement is projected onto a virtual plane at 2,100 m asl
905 (corresponding to an altitude of MC) at intervals of 5 mm. Solid and dashed contour lines
906 correspond to vertical uplift and subsidence, respectively. White, red, and gray circles
907 represent hypocenters determined by the KSVO for the periods from 1 January 2016 to

908 22 January 2018 (before the eruption), from 23 January to 22 April 2018 (after the
909 eruption), and from 22 to 23 April 2018 (representative of SPCG unrest in 2018),
910 respectively. Optimal crack parameters are summarized in the lower right of the figure.

911 The square with the dashed line represents the area shown in Fig. 6.

912

913 **Fig. 6** Spatial distribution of misfit values in horizontal and vertical cross-sections at
914 intervals of 100 m. For each panel, we fixed Z (horizontal cross-section), X (N–S cross-
915 section), and Y (E–W cross-section) to optimum values of 1100 m asl, 36.629° (latitude),
916 and 135.540° (longitude), respectively. Using the same method as in section 3.2, we
917 searched for the best-fit parameters L, A, D, U, and location (X and Y for horizontal cross
918 section, Y and Z for N–S cross-section, and X and Z for (E–W cross-section) within the
919 range described in section 3.2. Yellow lines are topographic contours at intervals of 20 m.
920 Yellow squares indicate the locations of craters formed during the 2018 eruption. White
921 and red circles represent hypocenters determined by the KSVO for the periods from 1
922 January 2016 to 22 January 2018 (before the eruption) and from 23 January to 22 April
923 2018 (after the eruption), respectively.

924

925 **Fig. 7** Comparison of observed (red arrows) and modeled (blue arrows) tilt vectors of
926 phase 2 (Fig.3). The location of the modeled crack is represented by the yellow rectangle.
927 Modeled vertical displacement is projected onto a virtual plane at 2100 m asl
928 (corresponding to an altitude of MC) at intervals of 1 mm. Solid and broken contour lines
929 correspond to vertical uplift and subsidence, respectively. White, red, and gray circles
930 represent hypocenters determined by the KSVO for the period from 1 January 2016 to 22
931 January 2018 (before the eruption), from 23 January to 22 April 2018 (after the eruption),
932 and from 22 to 23 April 2018 (representative of SPCG unrest in 2018), respectively.
933 Vertical N–S and E–W cross-sections of hypocenters are also shown. The optimal
934 dislocation of the crack is shown at lower right in the figure; other crack parameters are
935 as in Fig. 5.

936

937 **Fig. 8** Tracks of the ash cloud. Red bars represent ash height detected by the Nagano
938 weather radar (blue circle in Fig. 1a) at 2, 5, and 7 km from the MC at 10:05–10:10 (JST)
939 (Meteorological Research Institute 2018). Geometries of a buoyant plume were

940 calculated with Eqs 1 and 2, assuming a wind speed of 20 m/s (solid lines) and 30 m/s
941 (dashed lines). Values in the figure indicate the heat discharge rate \dot{q} in GW (10^9 W), as
942 defined in Equation (2). The source of the plume is fixed to the location of the MC.

943

944 **Fig. 9** Schematic diagram of the hydrothermal system associated with the 2018 MPCG
945 eruption. HF clusters represent hypocenter distributions of high frequency volcanic-
946 tectonic earthquakes. The depth of the self-sealed brittle–ductile transition zone is based
947 on the hypocenter distribution (Figs 5–7). ¹⁾ Matsunaga et al. (2020); ²⁾ Tseng et al. (2020);
948 ³⁾ Yamada et al. (2021); ⁴⁾ Ohba et al. (2019); ⁵⁾ Himematsu et al. (2020).

949

950 **Fig. 10** Comparison of observed (red arrows) and modeled (blue arrows) tilt vectors on
951 27 May 2011. **a** Inflation phase and **b** deflation phase. The location of the modeled crack
952 is represented by the yellow rectangle. Modeled vertical displacement is projected onto a
953 virtual plane at 2,100 m asl (corresponding to an altitude of MC) at intervals of 0.2 mm
954 and 0.07 mm, respectively. Solid and dashed contour lines correspond to vertical uplift
955 and subsidence, respectively. Crack parameters such as X, Y, Z, L, A, and D are the same

956 as for Fig. 5.

957

958 **Fig. S1** Comparison of observed (red arrows) and modeled (blue arrows) tilt vectors of
959 phase 1 (Fig. 3), assuming $L/W = \mathbf{a}$ 0.5, \mathbf{b} 1, and \mathbf{c} 4. The location of the modeled crack
960 in each case is represented by yellow rectangles. Modeled vertical displacement is
961 projected onto a virtual plane at 2,100 m asl (corresponding to the altitude of the MC).
962 Solid and dashed contours correspond to vertical uplift and subsidence, respectively.
963 Optimum crack parameters are summarized at lower right in each diagram. The optimal
964 length (L), width (W) (assumed as half of the horizontal length), and dislocation (U)
965 resulted in calculated volumetric expansions of $\sim 2.8 \times 10^5 \text{ m}^3$ ($L/W = 0.5$), $\sim 6.4 \times 10^5$
966 m^3 ($L/W = 1$), and $\sim 4.2 \times 10^5 \text{ m}^3$ ($L/W = 4$), respectively.

967

968 **Fig. S2** Inflation source during the 2014 unrest of the SPCG from March 2014 to October
969 2015. Optimal crack parameters are summarized at lower right in the figure. We searched
970 for the best-fit combination of four parameters (Z, L, A, and U), assuming a sill-like
971 source ($D = 0^\circ$) and $L/W = 2$. The latitude and longitude of the center of the sill were

972 fixed at 36.645° and 138.538°, respectively, representing the center of Mizugama crater.

973 In this analysis, the smallest misfit (root mean square sum of the difference between the

974 observed and calculated values of each tilt vector, and each uplift at KSYG (44 mm) and

975 KSE (25 mm) measured by GNSS) was calculated by the grid-search method as described

976 in Section 3.2. The optimal length (L), width (W), and dislocation (U) were 480 m, 240

977 m (assumed as half of the horizontal length), and 1.00 m, respectively, which resulted in

978 a calculated volumetric expansion of $\sim 1.2 \times 10^5 \text{ m}^3$.

979

980

981

EOF

Figures

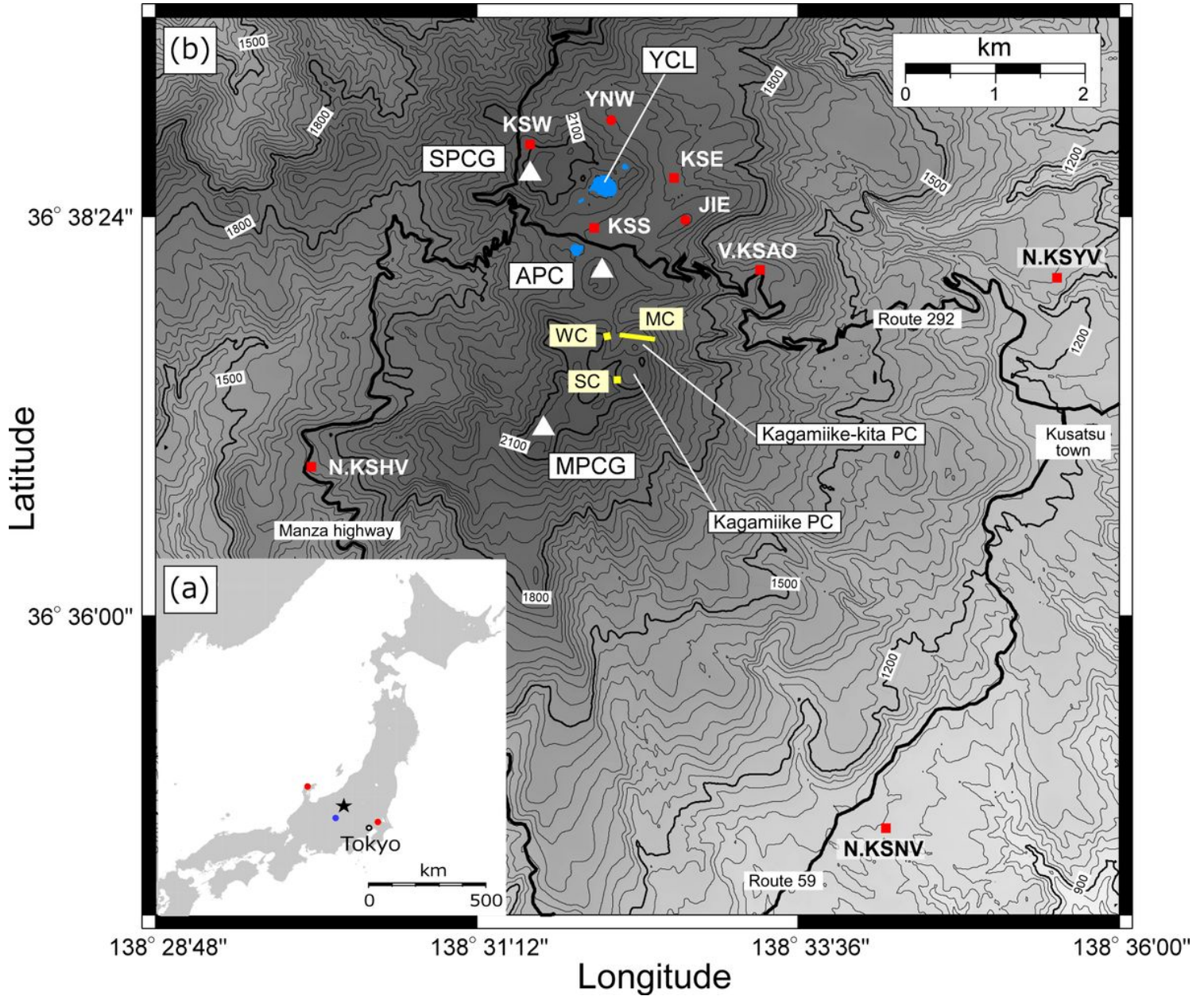


Figure 1

Location and topography of Kusatsu–Shirane volcano. a Location map of Kusatsu–Shirane volcano in Japan (star). Blue and red circles represent the locations of the Nagano weather radar site and an aerological observatory using a balloon and radiosonde, respectively (both operated by the Japan Meteorological Agency). b Topographic map of Kusatsu–Shirane volcano. Solid lines are topographic contours at intervals of 30 m. Red squares and circles indicate the locations of tiltmeters installed at the bottom of boreholes and at a depth of 1–2 m from the ground surface, respectively (Table 1). Yellow squares (MC, WC, and SC) indicate the locations of craters that formed during the 2018 eruption. PC = pyroclastic cone; MPCG = Motoshirane Pyroclastic Cone Group; SPCG = Shirane Pyroclastic Cone Group; YCL = Yugama Crater Lake; MC = main crater; WC = west crater; SC = south crater.

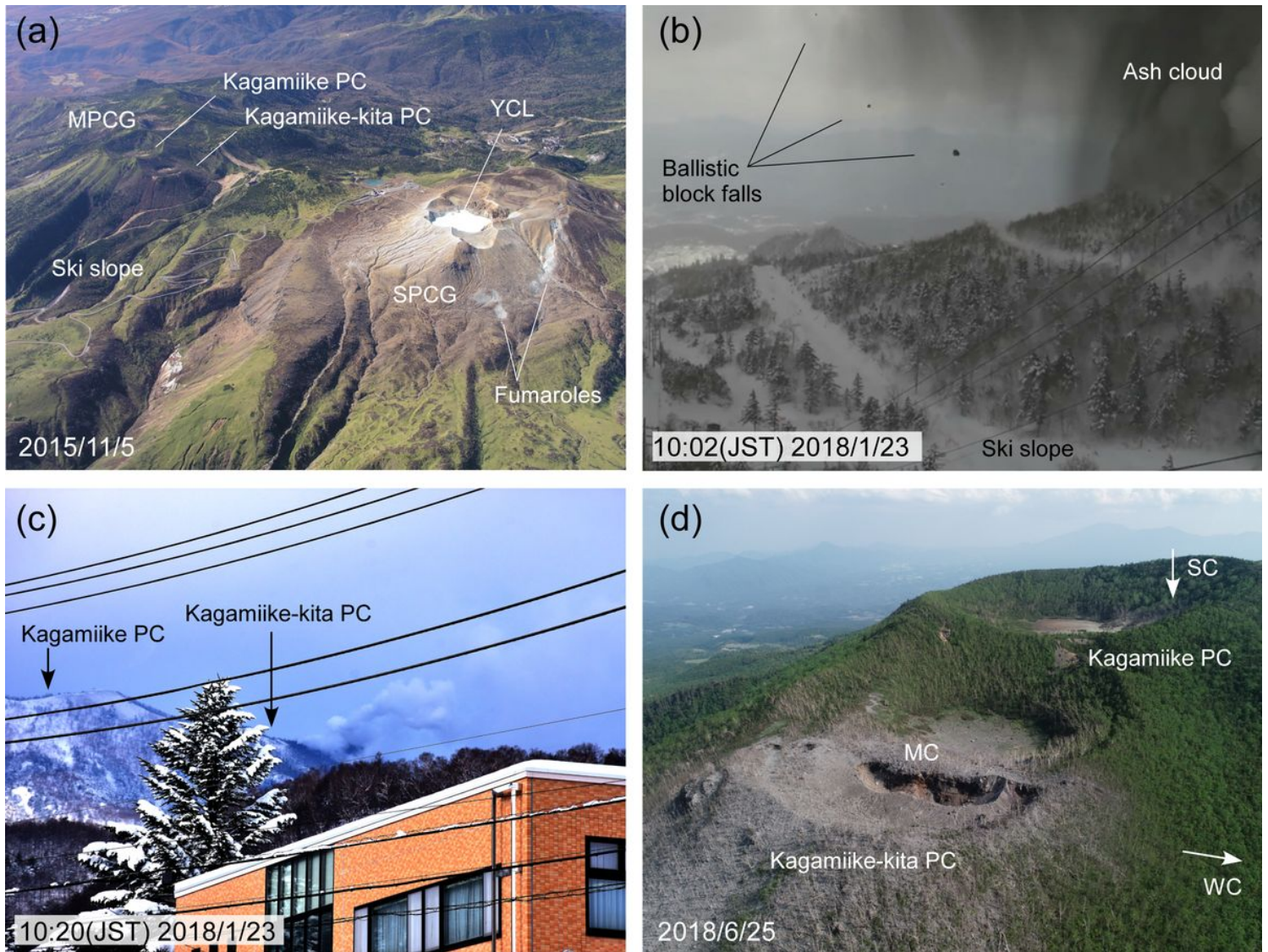


Figure 2

a Aerial photograph of Kusatsu–Shirane volcano (taken on 5 November 2015). PC = pyroclastic cone; MPCG = Motoshirane Pyroclastic Cone Group; SPCG = Shirane Pyroclastic Cone Group; YCL = Yugama Crater Lake. b Eruption cloud and ballistic block falls hitting the ski slope, (photograph taken by the Kusatsu Tourism Cooperation at 10:02 JST on 23 January 2018). c Weak volcanic cloud rising from Kagamiike-kita PC at about 10:20 JST on 23 January 2018. d Aerial photograph of the new main crater (MC) at Kagamiike-kita PC and south crater (SC) at Kagamiike PC formed during the 2018 eruption (photograph taken on 25 June 2018). The west crater (WC) is outside the photograph.

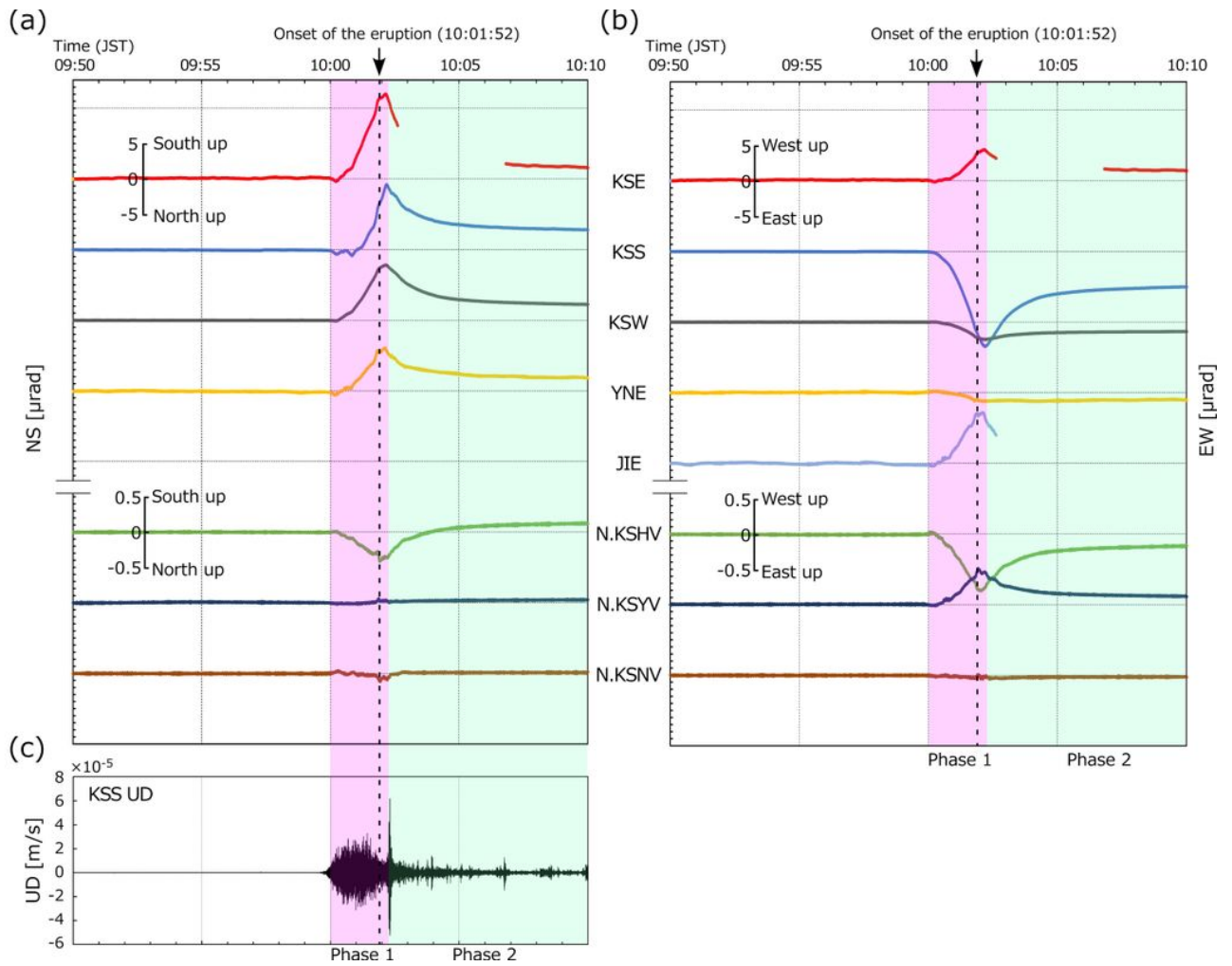


Figure 3

Tilt components recorded at 09:50–10:10 (JST) on 23 January 2018. a North–south and b west–east components. Acausal low-pass filters with cut-off frequencies of 0.034 and 0.021 Hz were applied to the tilt records of JTS-33 (KSE, KSS, KSW, N.KSHV, N.KSYV, and N.KSNV) and 701-2A (YNW and JIE), respectively. c Raw vertical ground velocity waveform at KSS. See Fig. 1 and Table 1 for station names and locations. We term the inflation and deflation phases as phase 1 and phase 2, respectively. The time of eruption onset was estimated by Yamada et al. (2021).

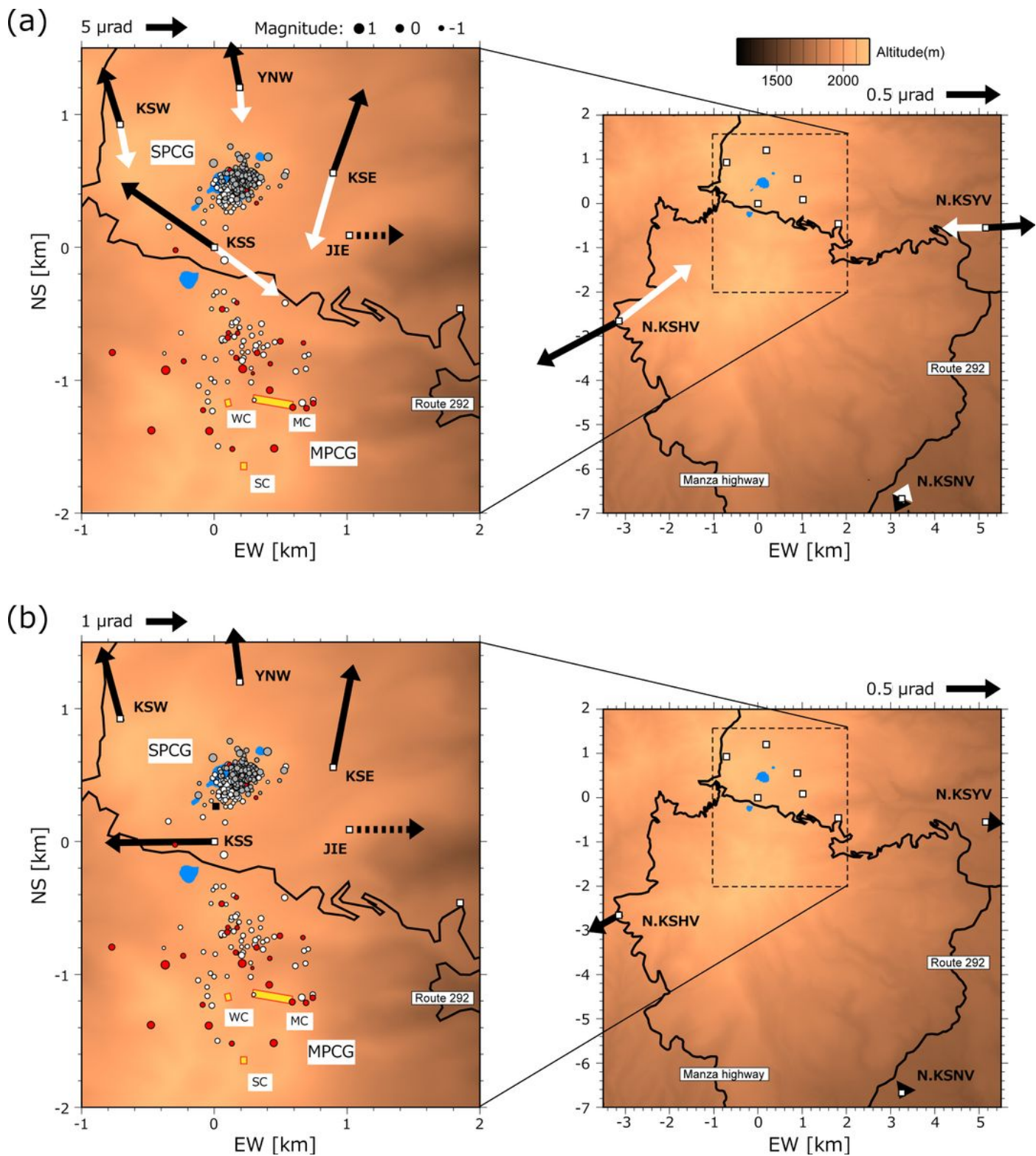


Figure 4

Tilt vectors in the study area. Yellow rectangles show the localities of vents formed during the 2018 eruption. White, red, and gray circles represent hypocenters for the periods from 1 January 2016 to 22 January 2018 (before the eruption), from 23 January to 22 April 2018 (after the eruption), and from 22 to 23 April 2018 (representative of SPCG unrest in 2018), respectively, as determined by the Kusatsu-Shirane Volcano Observatory, Volcano Fluid Research Center, Tokyo Institute of Technology. a Phase 1 (black

arrows, Fig.3) and phase 2 (white arrows, Fig.3). b First half of phase 1 (black arrows; 10:00–10:01 JST). Note that the vector scale is different from that in Fig. 4a.

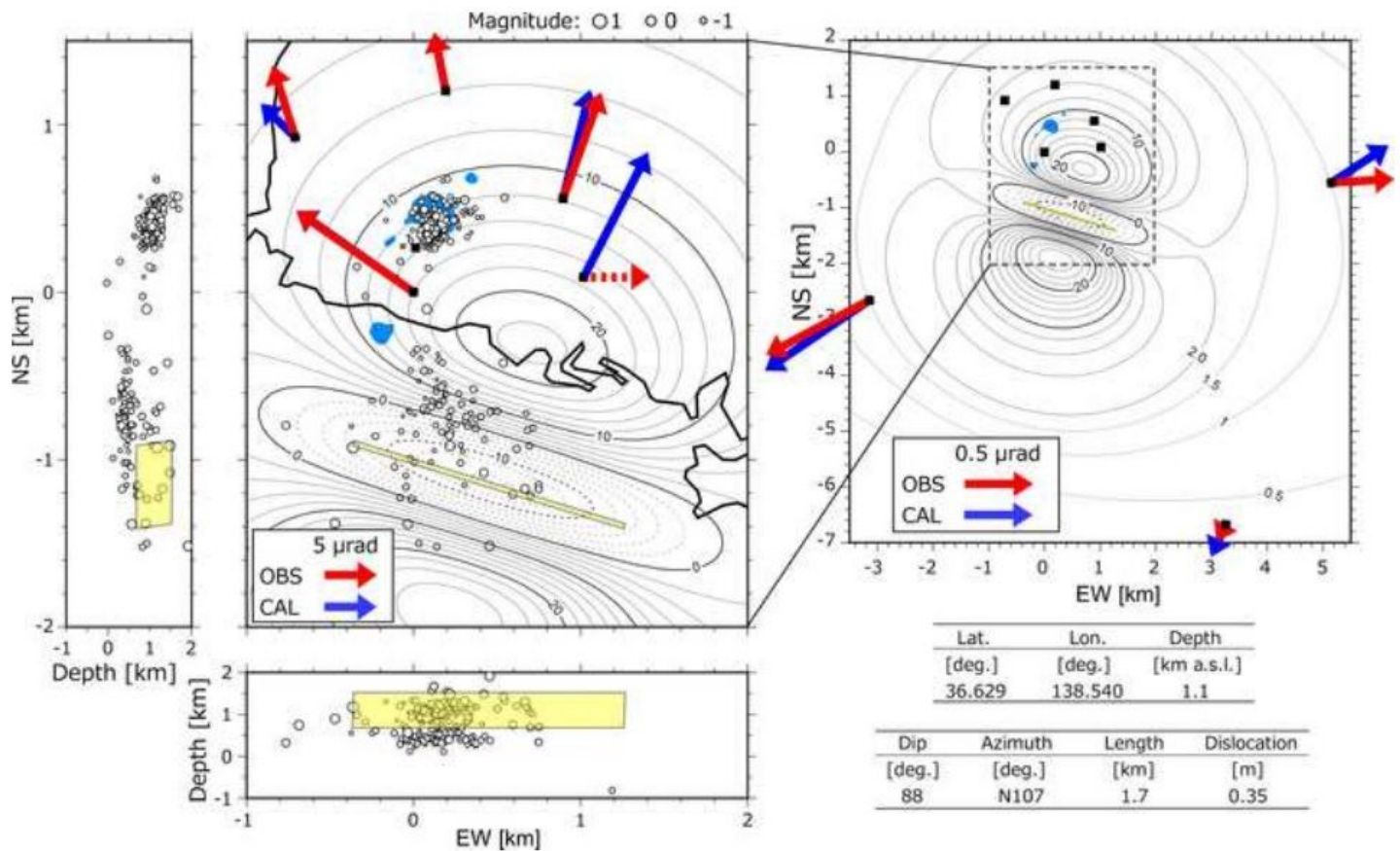


Figure 5

Comparison of observed (red arrows) and modeled (blue arrows) tilt vectors of phase 1 (Fig. 3). The location of the modeled crack is represented by the yellow rectangle. Modeled vertical displacement is projected onto a virtual plane at 2,100 m asl (corresponding to an altitude of MC) at intervals of 5 mm. Solid and dashed contour lines correspond to vertical uplift and subsidence, respectively. White, red, and gray circles represent hypocenters determined by the KSV0 for the periods from 1 January 2016 to 22 January 2018 (before the eruption), from 23 January to 22 April 2018 (after the eruption), and from 22 to 23 April 2018 (representative of SPCG unrest in 2018), respectively. Optimal crack parameters are summarized in the lower right of the figure. The square with the dashed line represents the area shown in Fig. 6.

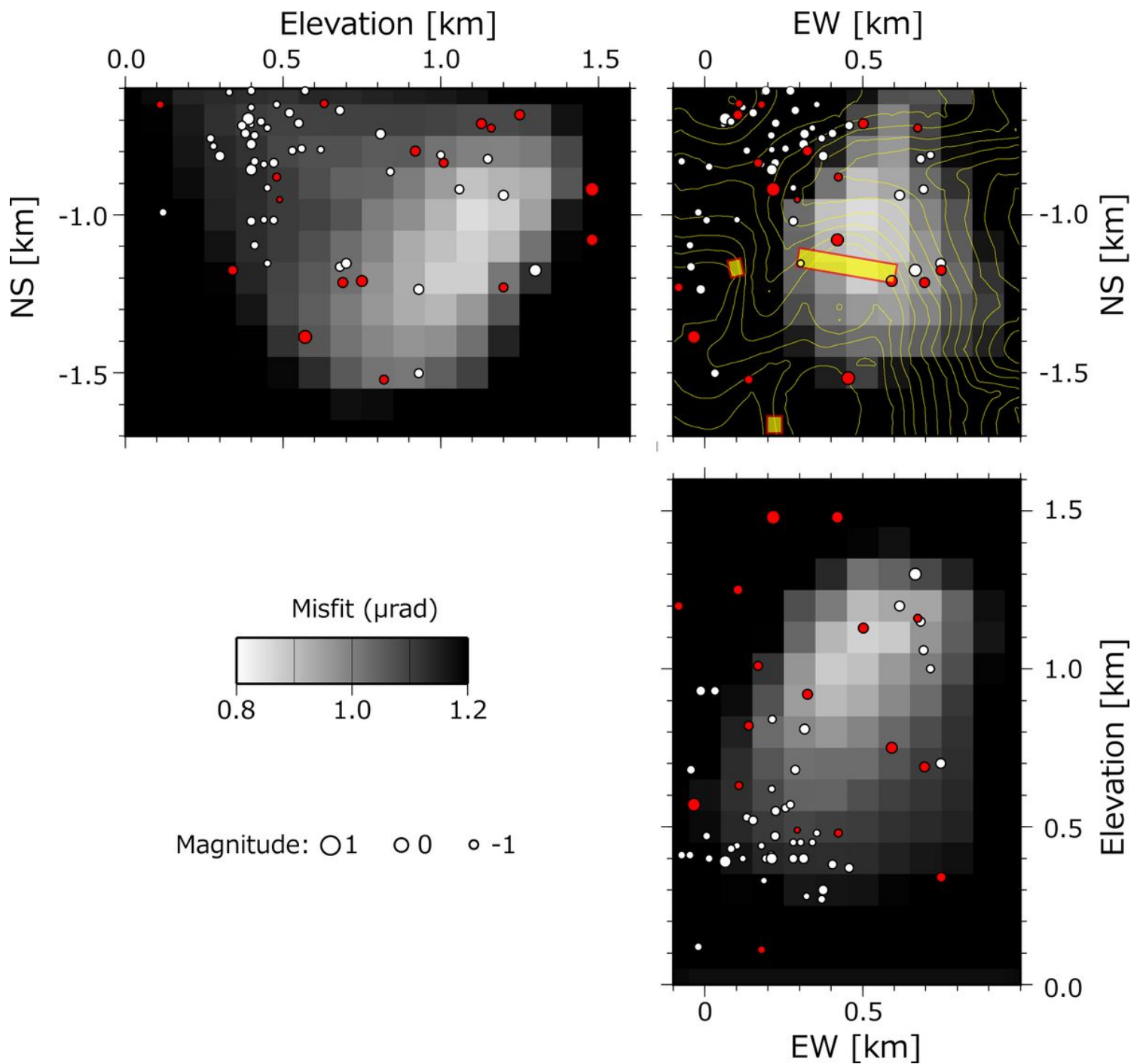


Figure 6

Spatial distribution of misfit values in horizontal and vertical cross-sections at intervals of 100 m. For each panel, we fixed Z (horizontal cross-section), X (N–S cross-section), and Y (E–W cross-section) to optimum values of 1100 m asl, 36.629° (latitude), and 135.540° (longitude), respectively. Using the same method as in section 3.2, we searched for the best-fit parameters L, A, D, U, and location (X and Y for horizontal cross section, Y and Z for N–S cross-section, and X and Z for (E–W cross-section) within the range described in section 3.2. Yellow lines are topographic contours at intervals of 20 m. Yellow squares indicate the locations of craters formed during the 2018 eruption. White and red circles represent

hypocenters determined by the KSV0 for the periods from 1 January 2016 to 22 January 2018 (before the eruption) and from 23 January to 22 April 2018 (after the eruption), respectively.

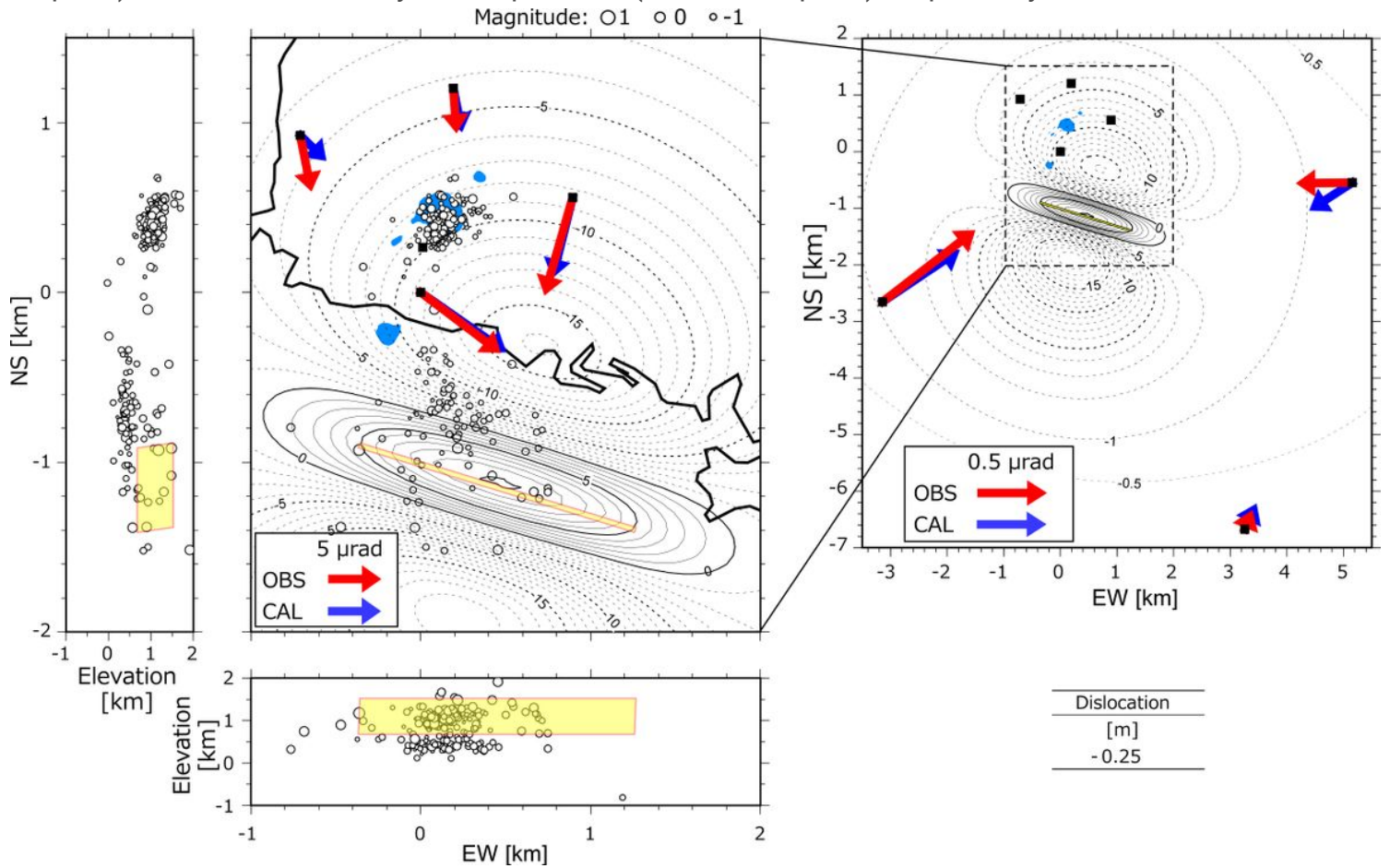


Figure 7

Comparison of observed (red arrows) and modeled (blue arrows) tilt vectors of phase 2 (Fig.3). The location of the modeled crack is represented by the yellow rectangle. Modeled vertical displacement is projected onto a virtual plane at 2100 m asl (corresponding to an altitude of MC) at intervals of 1 mm. Solid and broken contour lines correspond to vertical uplift and subsidence, respectively. White, red, and gray circles represent hypocenters determined by the KSV0 for the period from 1 January 2016 to 22 January 2018 (before the eruption), from 23 January to 22 April 2018 (after the eruption), and from 22 to 23 April 2018 (representative of SPCG unrest in 2018), respectively. Vertical N–S and E–W cross-sections of hypocenters are also shown. The optimal dislocation of the crack is shown at lower right in the figure; other crack parameters are as in Fig. 5.

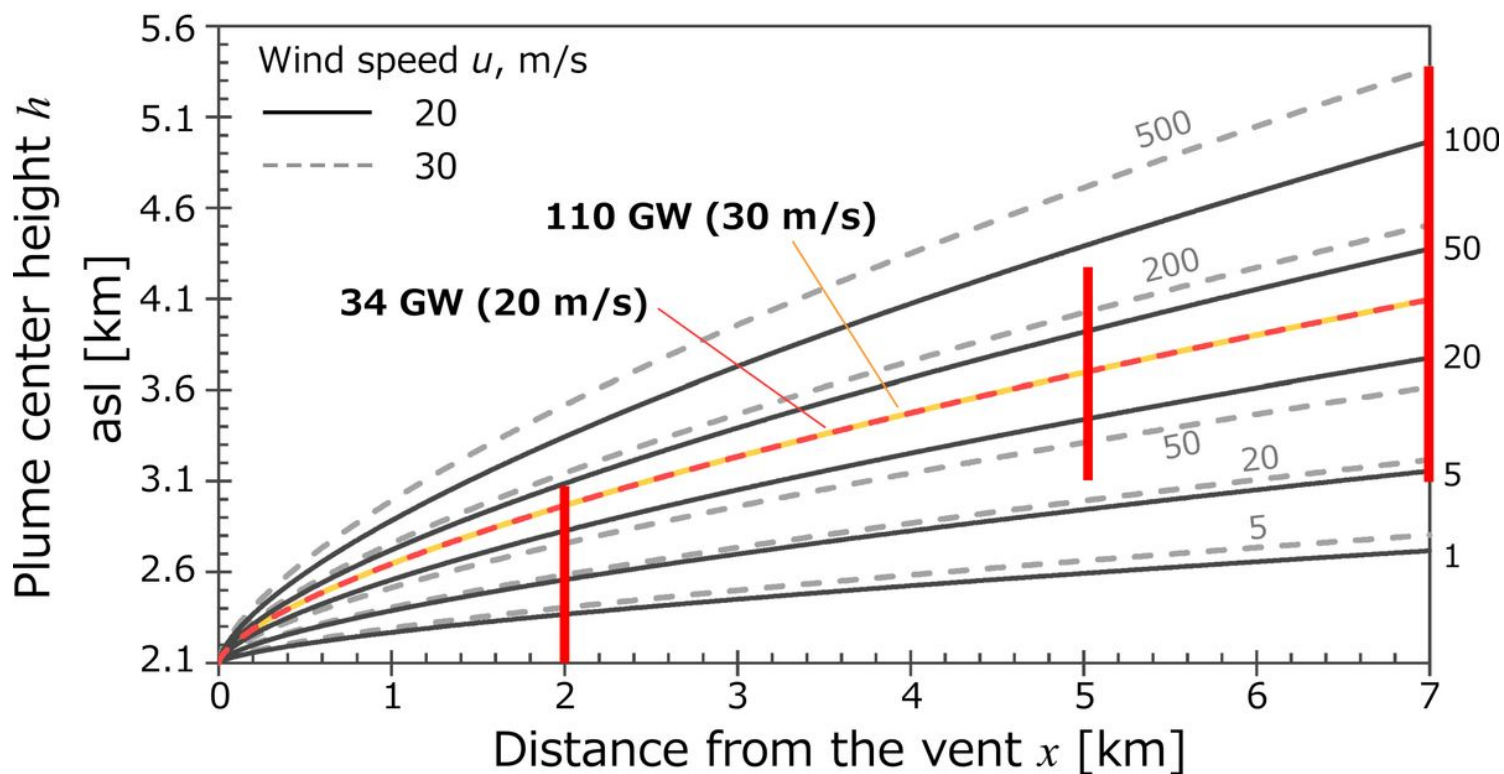
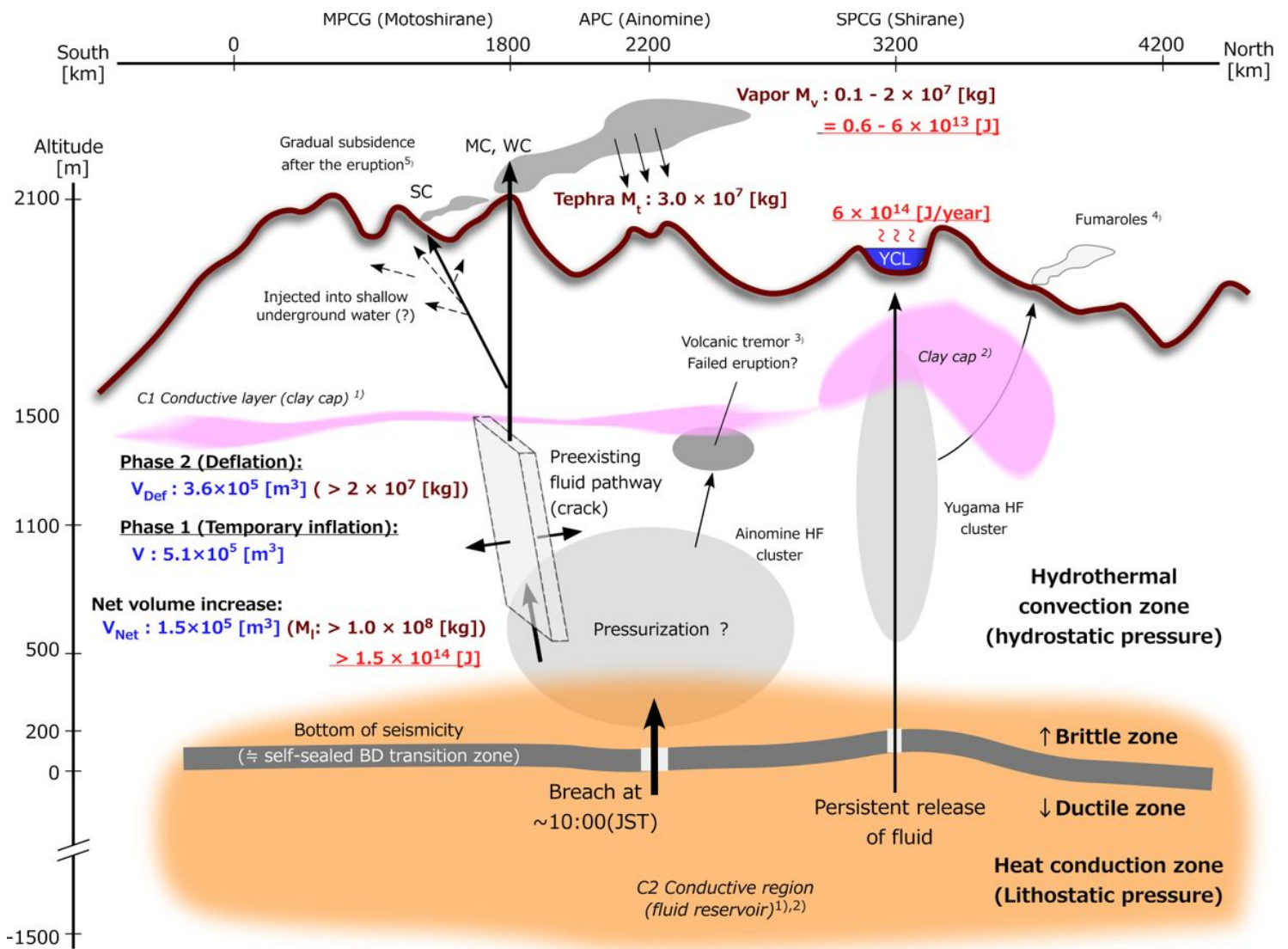


Figure 8

Tracks of the ash cloud. Red bars represent ash height detected by the Nagano weather radar (blue circle in Fig. 1a) at 2, 5, and 7 km from the MC at 10:05–10:10 (JST) (Meteorological Research Institute 2018). Geometries of a buoyant plume were calculated with Eqs 1 and 2, assuming a wind speed of 20 m/s (solid lines) and 30 m/s (dashed lines). Values in the figure indicate the heat discharge rate q in GW (109 W), as defined in Equation (2). The source of the plume is fixed to the location of the MC.



V: Volume increase during phase 1, $V_{Net} + V_{Def}$, m³
 V_{Def} : Volume decrease during phase 2, m³
 V_{Net} : Net volume increase, $V - V_{Def}$, m³

M_v : Mass of vapor of a plume, kg
 M_l : Mass of V_{Net} , assuming a liquid water density, kg
 M_t : Mass of tephra deposits, kg

Figure 9

Schematic diagram of the hydrothermal system associated with the 2018 MPCG eruption. HF clusters represent hypocenter distributions of high frequency volcanic-tectonic earthquakes. The depth of the self-sealed brittle–ductile transition zone is based on the hypocenter distribution (Figs 5–7). 1) Matsunaga et al. (2020); 2) Tseng et al. (2020); 3) Yamada et al. (2021); 4) Ohba et al. (2019); 5) Himematsu et al. (2020).

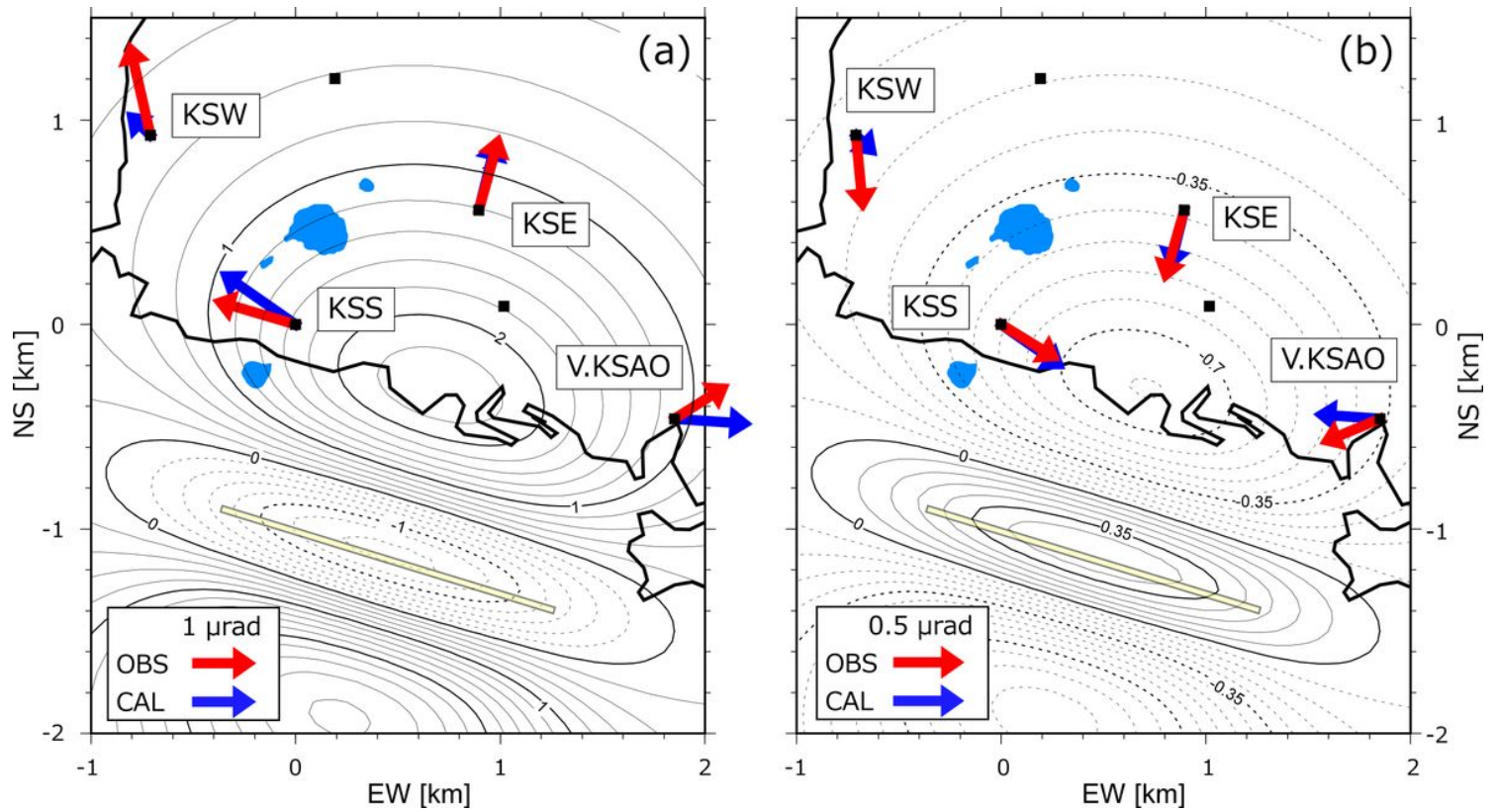


Figure 10

Comparison of observed (red arrows) and modeled (blue arrows) tilt vectors on 27 May 2011. a Inflation phase and b deflation phase. The location of the modeled crack is represented by the yellow rectangle. Modeled vertical displacement is projected onto a virtual plane at 2,100 m asl (corresponding to an altitude of MC) at intervals of 0.2 mm and 0.07 mm, respectively. Solid and dashed contour lines correspond to vertical uplift and subsidence, respectively. Crack parameters such as X, Y, Z, L, A, and D are the same as for Fig. 5.

Supplementary Files

This is a list of supplementary files associated with this preprint. Click to download.

- [FigS1aspect.jpg](#)
- [FigS2yugama.jpg](#)
- [GA.jpg](#)